medRxiv preprint doi: https://doi.org/10.1101/2022.03.04.22271927; this version posted March 8, 2022. The copyright holder for this preprint (which was not certified by peer review) is the author/funder, who has granted medRxiv a license to display the preprint in perpetuity. It is made available under a CC-BY-NC-ND 4.0 International license .

Proteogenomic analysis identifies the persistence of targetable lesions and proteomes through disease evolution in pediatric acute lymphoblastic leukemia

Amanda C. Lorentzian[1,2], Meiyun Guo[1,2], Enes K. Ergin[2,3], Neha M. Akella[1,2], Nina Rolf[1,2], C. James Lim[1,2], Gregor S.D. Reid[1,2], Christopher A. Maxwell[1,2,4], Philipp F. Lange[2,3,4]

Affiliations:

[1]Department of Pediatrics, University of British Columbia, Vancouver, CANADA

[2]Michael Cuccione Childhood Cancer Research Program at the BC Children's Hospital Research Institute, Vancouver, CANADA

[3]Department of Pathology, University of British Columbia, Vancouver, CANADA

[4]Correspondence to: Christopher A. Maxwell PhD
BC Children's Hospital
950 West 28th Avenue
Vancouver, BC
Canada V5Z 4H4
cmaxwell@bcchr.ca

Philipp F. Lange PhD
BC Children's Hospital
950 West 28th Avenue
Vancouver, BC
Canada V5Z 4H4
philipp.lange@ubc.ca

The authors declare no potential conflicts of interest

NOTE: This preprint reports new research that has not been certified by peer review and should not be used to guide clinical practice.

medRxiv preprint doi: https://doi.org/10.1101/2022.03.04.22271927; this version posted March 8, 2022. The copyright holder for this preprint (which was not certified by peer review) is the author/funder, who has granted medRxiv a license to display the preprint in perpetuity. It is made available under a CC-BY-NC-ND 4.0 International license .

ABSTRACT

Childhood acute lymphoblastic leukemia (ALL) genome landscapes indicate that relapses often arise from subclonal outgrowths. However, the impact of clonal evolution on the actionable proteome and response to targeted therapy is not known. Here, we present a comprehensive retrospective analysis of paired ALL diagnosis and relapsed specimen. Targeted next generation sequencing and proteome analysis indicated persistence of genome variants and stable proteomes through disease progression. Although variant-targeted therapies showed poor selectivity against viably-frozen tumor samples, paired samples showed high correlation of drug response. Proteome analysis prioritized PARP1 as a new pan-ALL target candidate; diagnostic and relapsed ALL samples demonstrated robust sensitivity to treatment with two PARP1/2 inhibitors. Together, these findings support initiating prospective precision oncology approaches at ALL diagnosis and emphasize the need to incorporate proteome analysis to prospectively determine tumor sensitivities, which are likely to be retained at disease relapse.

STATEMENT OF SIGNIFICANCE: We discover that disease progression and evolution in pediatric acute lymphoblastic leukemia is defined by the persistence of targetable genomic variants and stable proteomes, which reveal pan-ALL target candidates. Thus, personalized treatment options in childhood ALL may be improved with the incorporation of prospective proteogenomic approaches initiated at disease diagnosis.

INTRODUCTION

Relapsed cancer is a leading disease-related cause of death for children and adolescents (1). Targeting the specific molecular changes that arise in cancer cells may improve patient survival (2); for this reason, clinical trials centred on next generation sequencing (NGS)-based identification of biomarkers and targetable pathways are currently establishing patient enrolment strategies, clinical protocols, and critical safety data for personalized therapies. Most trials are currently limited to high-risk or recurrent disease. However, fast progressing disease often limits successful treatment options. In certain cases, precision oncology trials may be initiated at diagnosis. However, a major challenge for prospective precision oncology approaches is our limited understanding of lesion persistence or evolution, as tumour variants can be gained or lost at relapse.

medRxiv preprint doi: https://doi.org/10.1101/2022.03.04.22271927; this version posted March 8, 2022. The copyright holder for this preprint (which was not certified by peer review) is the author/funder, who has granted medRxiv a license to display the preprint in perpetuity. It is made available under a CC-BY-NC-ND 4.0 International license .

There is now a wealth of publicly available data for genomic characterization of paired diagnosis and relapse specimens from children with cancer. Clonal evolution does occur in pediatric leukemia wherein a minor clone, present only at low frequencies at diagnosis, is selected at time of relapse (3,4). While these studies show evolution in single nucleotide variants, often through chemotherapy-induced mutation (5), structural variants change less frequently with leukemia progression.

Few studies have yet investigated how protein levels change from diagnosis to relapse, especially pertaining to therapeutic targets. A previous proteomic analysis of matched diagnostic and relapsed B-cell precursor acute lymphoblastic leukemia (ALL) specimens, sourced from pediatric and adult patients, observed increased protein levels in specific pathways at relapse, including glycoloysis, phosphate pentose pathway and metabolic pathways that may contribute to chemo-resistance (6). Since proteins are the actual therapeutic targets (7,8), it is crucial to better understand the pediatric tumor proteome to determine how the response to therapy may change through progression. Here, we present a comprehensive interrogation of ALL proteogenome dynamics from diagnosis to relapse in paired patient specimens, specifically to understand how cancer-driving and potentially targetable lesions persist or differentiate through disease progression.

RESULTS

NGS reveals stability of affected genes through ALL disease progression

To examine proteogenomic evolution in pediatric ALL, we sourced paired initial diagnosis (Dx) and relapse (R) bone marrow mononuclear cells from patients (n=11) or non-cancer pediatric participants (n=3) seen at BC Children's Hospital (BCCH) (Supplementary Table S1). We first explored the mutational landscape via targeted, pediatric cancer-focused NGS analysis in paired progression samples (n=10 B-ALL, n=1 T-ALL) (9). Across the BCCH cohort, we detected recurrent copy number variants (CNV) or single nucleotide variants (SNV) in *CDKN2A/B*, *NRAS, KRAS, IKZF, JAK1,* and *JAK2* (Fig. 1A, Supplementary Fig. S1 and Supplementary Table S2), which are commonly mutated in pediatric ALL samples (8). Nine of the eleven patients had at least 50% retention of mutations and four of these patients had 100% retention of mutations.

medRxiv preprint doi: https://doi.org/10.1101/2022.03.04.22271927; this version posted March 8, 2022. The copyright holder for this preprint (which was not certified by peer review) is the author/funder, who has granted medRxiv a license to display the preprint in perpetuity. It is made available under a CC-BY-NC-ND 4.0 International license .

Figure 1: NGS reveals stability of affected genes through ALL disease progression

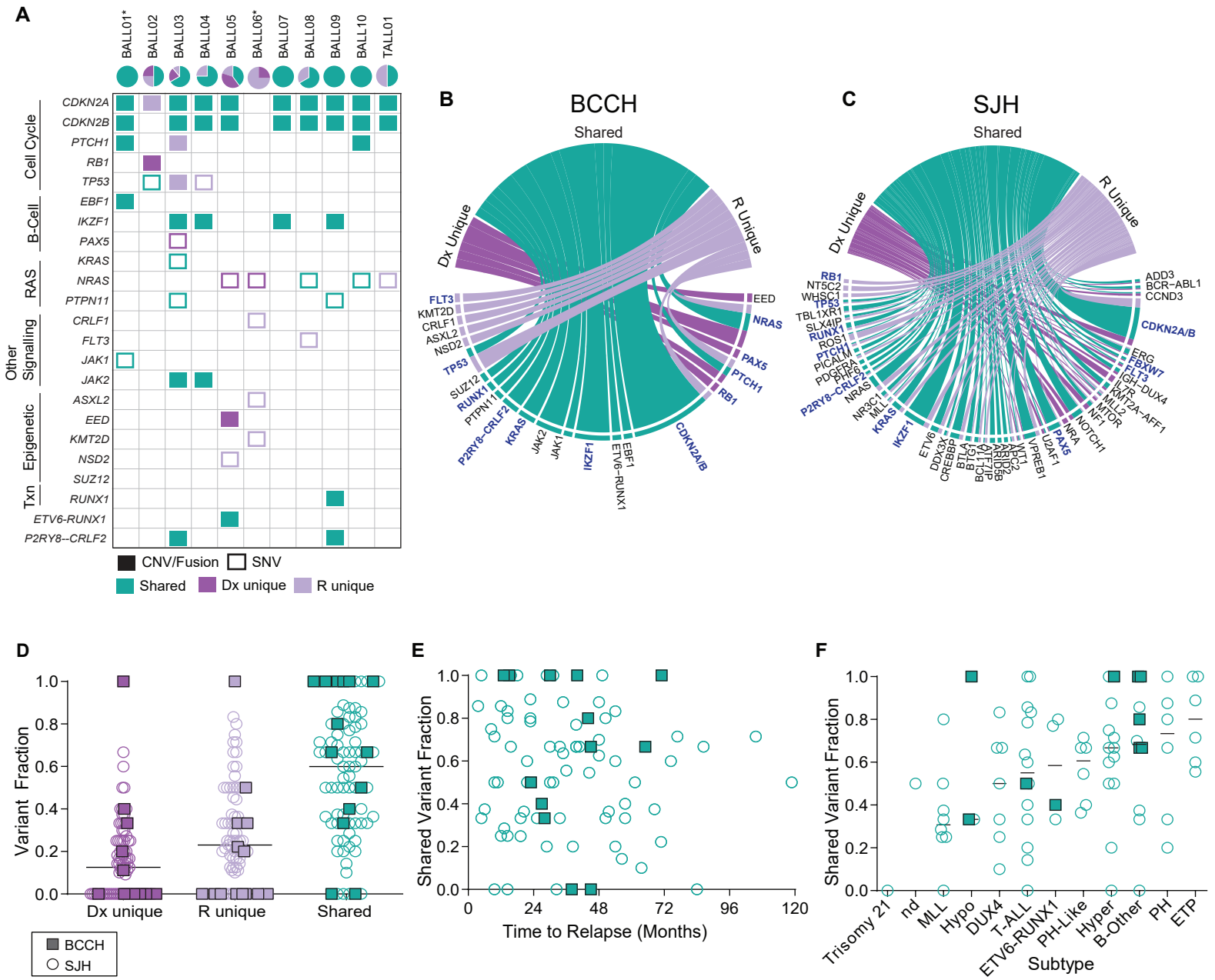

Figure 1: NGS reveals stability of affected genes through ALL disease progression

A. Mutated gene products identified through targeted DNA/RNA-fusion sequencing of paired diagnosis (Dx) and relapse (R) samples. Mutations detected in both Dx and R samples are represented by green boxes, mutations unique to Dx are dark purple, and R unique are light purple. CNVs are full boxes and SNVs are outlined boxes. The pie diagrams at the top summarize the number of mutations for each category for each patient. An asterisk indicates multi timepoint patients; BALL01 R2-R3-R4-R5-R5P, BALL02 Dx-R1-R2.

B. Circos plot for all mutations identified in the BCCH cohort demonstrating mutations that were Dx unique, R unique, or shared between Dx and R samples.

C. Circos plot for all mutations identified in the SJH cohort demonstrating mutations that were Dx unique, R unique, or shared between Dx and R samples.

D. Fraction of variants identified as D unique, R1 unique, or shared within paired samples sourced from 80 ALL patients (n= 11 from BCCH represented by squares, n= 69 from SJH represented by circles). The black bar represents the median of the population.

E. Dot plot for fraction of shared variants versus time to relapse for 80 ALL patients (n= 11 from BCCH represented by squares, n= 69 from SJH represented by circles).

F. Dot plot for fraction of shared variants separated by disease subtype for 80 ALL patients (n= 11 from BCCH represented by squares, n= 69 from SJH represented by circles). The black bar represents the median of the population.

medRxiv preprint doi: https://doi.org/10.1101/2022.03.04.22271927; this version posted March 8, 2022. The copyright holder for this preprint (which was not certified by peer review) is the author/funder, who has granted medRxiv a license to display the preprint in perpetuity. It is made available under a CC-BY-NC-ND 4.0 International license .

The majority was retained from Dx to R: nine of the eleven patients had at least 50% retention of mutations and four of these patients had 100% retention of mutations, indicating high stability of lesions in this cohort.

At time of relapse of pediatric ALL, clonal evolution frequently includes the outgrowth of clones defined by a different mutational site within the same affected gene; for example, a relapse clone with KRAS.A146T replaces the diagnostic KRAS.G12D clone (3). Since alternate pathogenic mutations in the same gene often serve as biomarkers for the same targeted treatment, we focused our analysis on the affected gene, rather than the mutation site. We evaluated the detected lesions grouped by detection only at diagnosis (Dx unique), only at relapse (R unique), or at both timepoints (shared). Here we found 67% (30 of 45) of affected genes were shared between paired diagnosis and relapse samples in the BCCH cohort (Fig. 1B). To determine the generalizability of this finding, we mined public NGS datasets from ALL cases (n=49 B-ALL; n=20 T-ALL) treated at St. Jude's Hospital (SJH) (Supplementary Table S3) (10). Consistently, genes found to be mutated at diagnosis were most often also mutated at relapse in B-ALL and T-ALL patients, including several known pediatric cancer-driving genes (Fig. 1C and Supplementary Fig. S2). Samples collected from BCCH and SJH showed similar distributions of affected genes that were shared between time-points or were unique to Dx or R (Fig. 1C,D and Supplementary Table S4), with the majority of variants shared between paired diagnosis and relapse samples (Fig. 1C). In fact, the genes that were persistently mutated through disease progression were highly similar in both cohorts, including *CDKN2A/B, IKZF1,* and *N/KRAS*, with structural variants being retained with higher frequency than SNVs (Supplementary Fig. S3A-C). Surprisingly, retention of genetic lesions was not correlated with the time between diagnosis and first relapse, or between relapses. (Fig. 1E and Supplementary Fig. S3D,E). However, we observed relatively higher stability for Hyperdiploid (hyper), Philadelphia + (PH), and early T-cell precursor (ETP) sub-types (Fig. 1E).

Matched patient-derived leukemic cells respond similarly to variant-selected agents

Persistence of affected genes suggests that sensitivity to precision therapies may also persist with disease progression. To examine this, we paired affected genes with targeted agents following the Pediatric MATCH strategy and evidence from clinical trials or case reports, as described (9).

medRxiv preprint doi: https://doi.org/10.1101/2022.03.04.22271927; this version posted March 8, 2022. The copyright holder for this preprint (which was not certified by peer review) is the author/funder, who has granted medRxiv a license to display the preprint in perpetuity. It is made available under a CC-BY-NC-ND 4.0 International license .

In the SJH and BCCH cohorts (n=80 paired samples), we found 64% of ALL patients (51 of 80) retained at least one variant-agent pairing at disease relapse; in fact, nearly 50% of patients (38 of 80) showed complete retention of variant-agent pairings through disease progression (Fig. 2A and Supplementary Table S5). Only six patients had variant-agent pairings unique to the diagnostic timepoint, while 10 patients harbored no targetable mutations (Fig. 2A).

We sourced viably-frozen paired bone marrow mononuclear cells (BM-MNC) from six patients treated at BCCH, including four paired BM-MNC that showed retention of all affected genes and two paired specimens with partial/no retention (Fig. 2B). Within this cohort, we identified four variant-agent pairings and then treated viable patient specimen with graded doses of a representative targeted agent (CDK4/6: palbociclib; MEK: Trametinib, JAK/STAT: Ruxolitinib; SMO: Vismodegib). We used image-based drug screening of B-ALL cells co-cultured with mesenchymal stromal cells (MSC) to determine IC50 values for each sample after exposure (for 48-72 hours) to the four different targeted agents (Fig. 2B). Overall, the measured IC50 values revealed poor selectivity, with predicted responses to trametinib being an exception. Trametinib IC50 values were lower for patient samples predicted to be sensitive to MEK inhibition (Fig. 2C). In contrast, Palbociclib IC50 values did not differ within the primary ALL cohort (Fig. 2C) suggesting cytotoxicity is induced in a non-targeted manner by this agent. Overall, the measured IC50 values in relapsed samples correlated with values measured in matched diagnostic samples (Pearson's r = 0.85, p = 6.0e-7, Fig. 2D). Therefore, our analysis reveals stability of actionable gene lesions as well as highly correlated, though poorly selective, drug sensitivities for matched pediatric ALL disease progression samples.

Proteome investigation of matched specimens reveals stable levels of cancer-associated proteins and processes.

Ultimately, drug sensitivity is determined by the state of the targeted and compensatory protein pathways. To determine whether the observed persistence of cancer-associated targetable genomic lesions and associated drug sensitivities can be generalized, we next questioned if the protein levels of pediatric cancer-associated proteins (CAPs) (Supplemental Table S6) follow the same trend. We employed a data independent acquisition approach (DIA) using a spectral library of 8183 proteins to examine six primary matched Dx-R or R-R sets (BALL01, BALL03,

medRxiv preprint doi: https://doi.org/10.1101/2022.03.04.22271927; this version posted March 8, 2022. The copyright holder for this preprint (which was not certified by peer review) is the author/funder, who has granted medRxiv a license to display the preprint in perpetuity. It is made available under a CC-BY-NC-ND 4.0 International license.

Figure 2: Matched patient-derived leukemic cells respond similarly to variant-selected agents

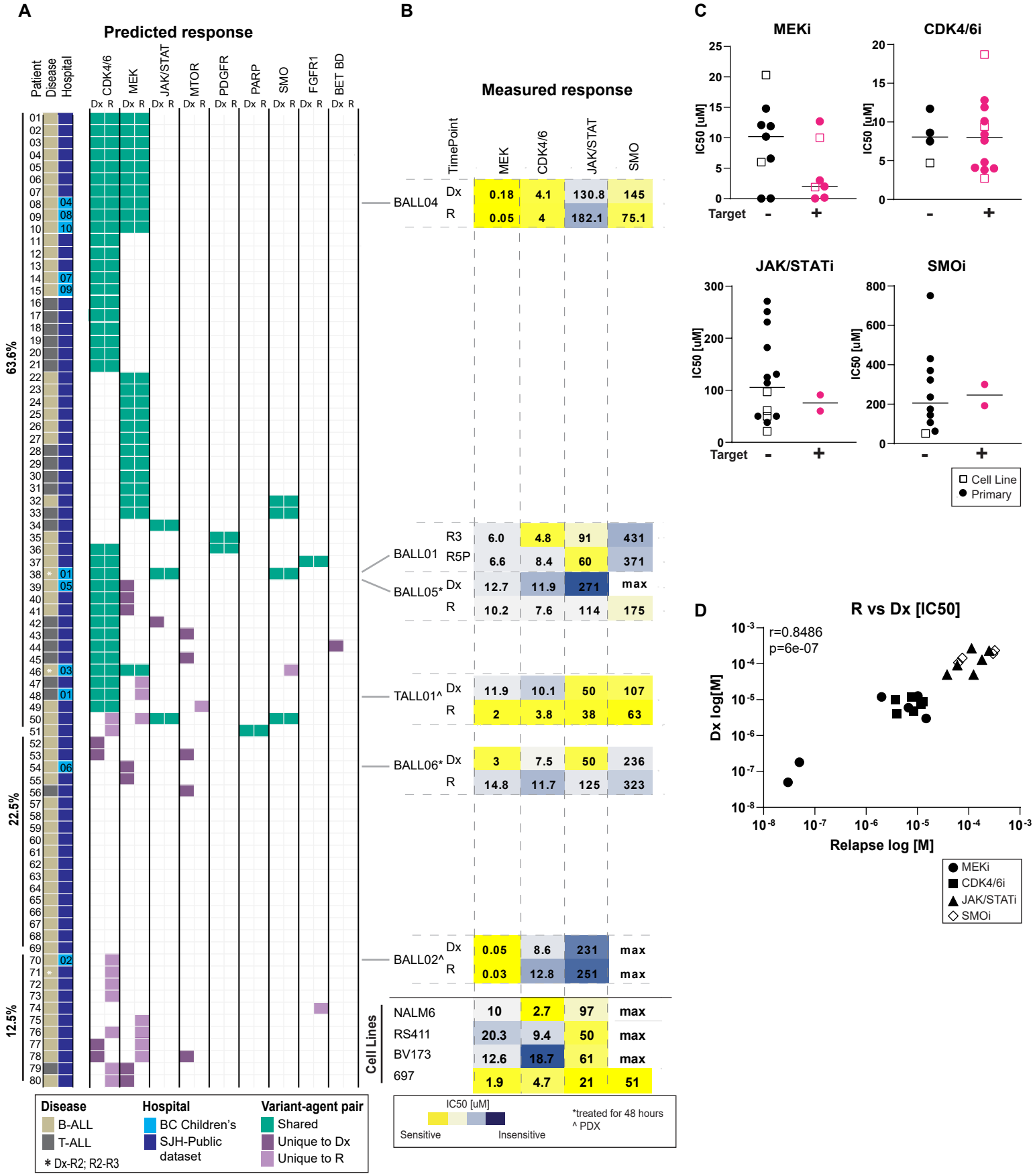

Figure 2: Matched patient-derived leukemic cells respond similarly to variant-selected agents

A. Predicted sensitivity to targeted agents in paired Dx-R samples (or Dx-R2, R2-R3 indicated by an asterisk) taken from 80 ALL patients treated at BCCH (n=11, light blue) or SJH (n=69, dark blue). B-ALL (light brown) and T-ALL (dark brown) samples are indicated. Shared variants (green), Dx unique variants (dark purple), or R unique variants (light purple) are indicated. Agent-variant pairs were assigned following the strategy outlined in the Pediatric Match Trial (9).

B. Measured IC50 values for viably frozen ALL samples from patients treated at BCCH (n= 6 patients) and representative cell lines. ALL samples were co-cultured with hTERT-MSCs and separately treated with four inhibitors, MEKi, CDK4/6i, JAK/STATi, and SMOi. IC50 [μM] are colored by most sensitive in yellow to least sensitive in blue. Measurements represent the mean of n=2 replica wells from a single experiment.

C. Dot plots for IC50 [μM] values measured for primary samples or cell lines for each drug. Samples are separated based on the presence (pink) or absence (black) of a genomic variant predicted to augment drug sensitivity.

D. Correlation of IC50 [M] values measured for paired Dx and R paired samples. Individual drugs are indicated by unique identifiers. r= Pearson correlation coefficient.

medRxiv preprint doi: https://doi.org/10.1101/2022.03.04.22271927; this version posted March 8, 2022. The copyright holder for this preprint (which was not certified by peer review) is the author/funder, who has granted medRxiv a license to display the preprint in perpetuity. It is made available under a CC-BY-NC-ND 4.0 International license .

BALL04, BALL05, BALL06, BALL07, one PDX-derived Dx-R-R set (BALL02), and three non-cancer bone marrow (BM) specimens (Supplementary Fig. S4, S5 and Supplementary Tables S7, S8). Across cases, we identified 45 CAPs to be significantly more abundant in diagnosis specimens (n = 6) or relapse specimens (n = 12) compared to non-cancer controls (n = 3) (Supplementary Fig. S6A-D and Supplementary Table S9). Of these 45 proteins, we identified several proteins that are commonly overexpressed in acute lymphoblastic leukemias such as FLT3, CDK6, and EBF1 (11). The majority (n = 36 proteins) showed increased abundance at both disease time-points (Fig. 3A) and their abundance levels were positively correlated between diagnosis and relapse (or relapse-relapse) (Pearson's r = 0.75, p<2.2e-16); similarly, proteins with lower abundance (n = 10 proteins in either disease state) showed significant positive correlation between disease states (Pearson's r = 0.70, p<3.5e-15) (Supplementary Fig. S6E-F). Restricting the comparisons to matched specimens (n = 7 patients) confirmed that the high correlation was retained at the level of individual patients (Fig. 3B, Pearson's r = 0.67 - 0.90. These initial findings showed stable levels of pediatric CAPs through disease progression.

After observing high stability of protein abundance in the subset of CAPs, we investigated the full proteome to better understand inter- and intra- patient stability among the disease states. We tested all possible patient and timepoint pairings for statistically significant equivalence. As expected, significant equivalence of protein abundance was lowest when proteomes of non-cancer specimens were compared to proteomes of cancer specimens (63% or 68% equivalent to Dx or R, respectively) (Fig. 3C and Supplementary Fig. S7A). In contrast, >90% of robustly quantified proteins showed equivalent abundance when comparing proteomes of diagnosis and relapse specimens, or multiple relapses, from the same patient (Fig. 3C, Supplementary Fig. S7B and Supplementary Table S10). Consistent with our analysis of genomic stability and CAP correlation, only BALL05 and BALL06 showed lower equivalence (59% and 69% respectively) (Fig. 3C). At only 75% (median equivalence), different patients at either diagnosis or relapse show significantly lower proteome equivalence than individual patients through progression (Fig. 3C).

To determine processes that are particularly stable throughout progression, we next performed a gene set and pathway enrichment analysis. Proteins found to be equivalent between cancer and

medRxiv preprint doi: https://doi.org/10.1101/2022.03.04.22271927; this version posted March 8, 2022. The copyright holder for this preprint (which was not certified by peer review) is the author/funder, who has granted medRxiv a license to display the preprint in perpetuity. It is made available under a CC-BY-NC-ND 4.0 International license .

Figure 3: Proteome investigation of matched specimens reveals stable levels of cancer associated proteins and processes are stable

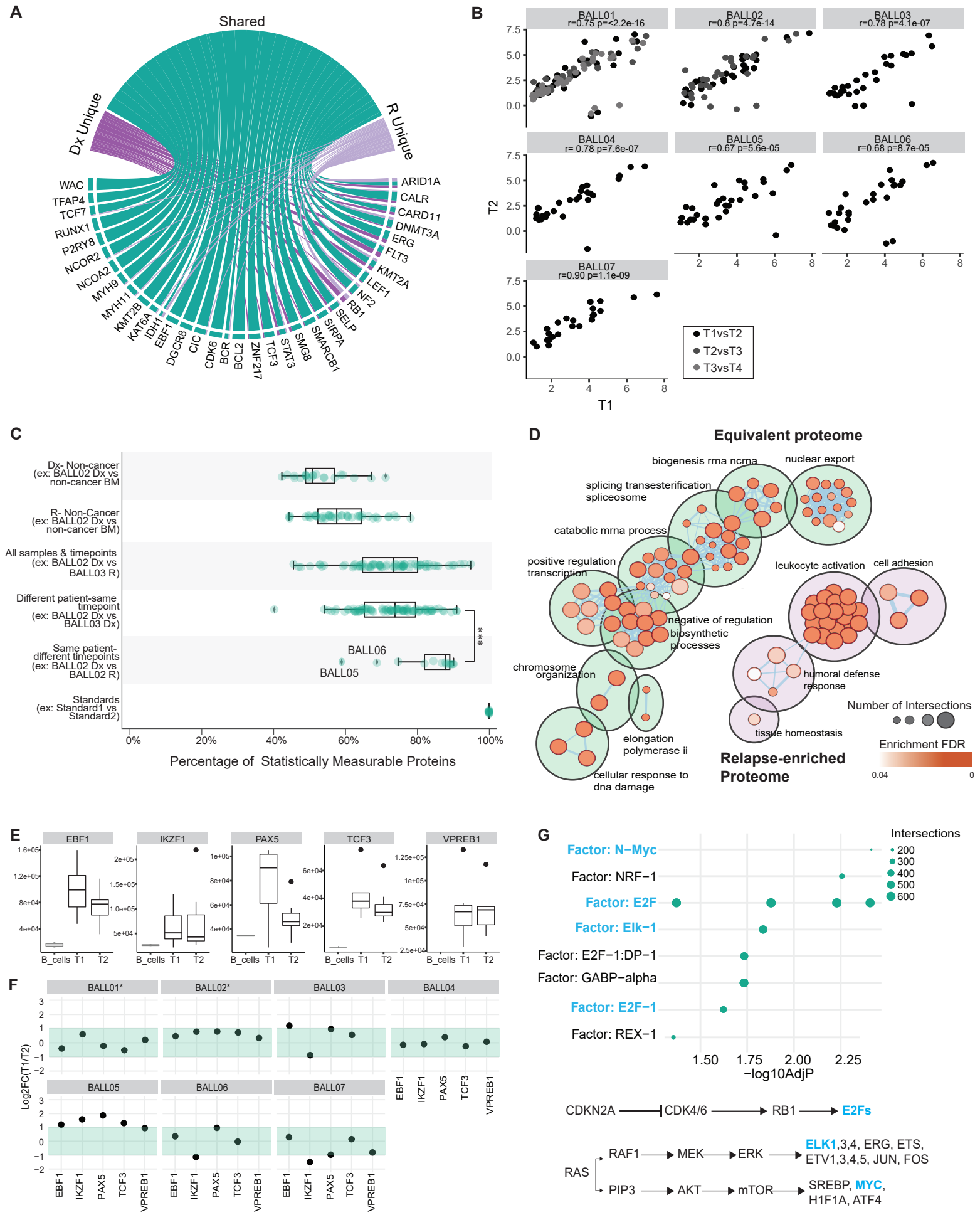

medRxiv preprint doi: https://doi.org/10.1101/2022.03.04.22271927; this version posted March 8, 2022. The copyright holder for this preprint (which was not certified by peer review) is the author/funder, who has granted medRxiv a license to display the preprint in perpetuity. It is made available under a CC-BY-NC-ND 4.0 International license .

Figure 3: Proteome investigation of matched specimens reveals stable levels of cancer-associated proteins and processes.

A. From the list of 269 pediatric cancer associated proteins (CAPs), 141 proteins were detected in our data and 45 proteins were deemed significant (LIMMA analysis of Initial Diagnosis (Dx) samples vs. non-cancer bone marrow (BM) samples and Relapse (R) vs non-cancer BM samples (log2FC>1, p-value adjusted BH-FDR<0.05). Circos plot summarizes significantly overexpressed cancer associated proteins (CAPs).

B. Of the 45 proteins that were overexpressed, the protein expression for each protein that was overexpressed at Dx, was plotted as timepoint 1 (T1) vs timepoint 2 (T2), where T1 is the earliest timepoint available for the specimen (calculated as the log2(protein expression/the average protein expression in the non-cancer BM)). Pearson's r correlation was calculated for all sample pairs. In cases that we had multiple time-points (BALL01 and BALL02) the correlation was calculated for consecutive pairings and are represented by the different colored dots.

C. Summary of tests for equivalence (Two-one-sided t-test (TOST) for equivalence, boundaries between log2FC<-1 and log2FC>1) of protein abundance between different groups and pairings. Only statistically measurable proteins are represented. Each dot represents the mean equivalence or difference of all protein abundance for a pairing. Significance is assigned by mann-whitney wilcoxon test, *** indicates p-value<=.0001.

D. Pathway enrichment analysis of the stable population of proteins represented in green and relapse enriched population of proteins represented in purple. The color of the circles indicates the enrichment FDR and size represents the number of identifications for the term.

E. Abundance of transcription factors of interest for each sample separated by timepoint (T1 or T2, black) compared to protein expression in mature B-cells (n=2 samples) isolated from peripheral blood mononuclear cells (grey).

F. Dot plots represent the log2FC of timepoint 1(T1)/timepoint 2(T2) for each of the proteins for each sample. The shaded green area indicates the stable range of -1 to 1FC. *For patients with multiple timepoints (BALL01 and BALL02) only the log2ratio of the earliest timepoint/the latest timepoint is represented for simplicity.

G. Enriched transcription factor (TF) motifs by FDR-adjusted log10 p-value. Light blue text indicates TFs that are regulated by CDK4/6 and MEK pathway. Simplified diagrams of these pathways are demonstrated below

medRxiv preprint doi: https://doi.org/10.1101/2022.03.04.22271927; this version posted March 8, 2022. The copyright holder for this preprint (which was not certified by peer review) is the author/funder, who has granted medRxiv a license to display the preprint in perpetuity. It is made available under a CC-BY-NC-ND 4.0 International license .

non-cancer were removed prior to the enrichment analysis to eliminate 'housekeeping' mechanisms. Pathway enrichment analysis identified processes linked to overall cell survival as equivalent amongst cancer proteomes, including transcription related processes, metabolic processes, and cellular responses to DNA (Fig. 3D and Supplementary Table S11). Within the small set of proteins that differed between diagnosis and relapse, no enriched terms specific to the diagnostic timepoint could be identified. At relapse, processes involving cell adhesion, indicating more motility and proliferative mechanisms, and immune response (leukocyte activation, neutrophil activation involved in immune response, granulocyte activation, and exocytosis, among others) were found enriched (Fig. 3D and Supplementary Table S12). We next probed proteins involved in B-cell development, IKZF1, EBF1, PAX5, VPREB1, and TCF (12), that are commonly dysregulated in ALL. Overall abundance of these proteins was significantly higher in cancer samples than in mature B-cells isolated from non-cancer peripheral blood mononuclear cells (PBMCs) (Fig. 3E and Supplementary Table S13). Moreover, for most patients, stable abundance was observed between disease states (Fig. 3E, F).

Finally, we examined transcription factor (TF) motifs associated with the regulation of genes encoding for equivalent proteins and identified enrichment of motifs relating to the E2Fs, ELK-1 and MYC transcription factors (Fig. 3G and Supplementary Table S14). Importantly, these TFs are primarily activated by the CDK4/6 and MEK pathways (Fig. 3G). Consistently, genomic deletion of CDKN2A (11 of 14 samples) and RAS activating mutations (8 of 14 samples) were recurrent in the BCCH cohort, as previously described in Fig. 1A. Overall, pathway enrichment analysis characterized proliferative and transcriptionally active pathways to be stable during disease progression. Furthermore, we observed stable expression of keystone proteins and the enrichment of transcription factors that are directly influenced by stable and recurrent genetic lesions.

Whole proteome discovery-driven analysis identifies pan-ALL protein targets

The measured cytotoxicity was disappointing for agents informed by the Pediatric Match genetic variant-agent prioritization strategy (Fig. 2C) leading us to probe our proteome datasets for new targets. To discover pan-ALL protein targets, we first filtered for proteins identified in more than 40% of specimens and with a high overall abundance (log10 intensity) and strong abundance

medRxiv preprint doi: https://doi.org/10.1101/2022.03.04.22271927; this version posted March 8, 2022. The copyright holder for this preprint (which was not certified by peer review) is the author/funder, who has granted medRxiv a license to display the preprint in perpetuity. It is made available under a CC-BY-NC-ND 4.0 International license .

increase over non-cancer (log2 FC) (cut-off: at least 95th percentile for both metrics) (Fig. 4A). We defined stable protein abundance between paired diagnostic and relapsed samples as a model variable for target discovery; using this criterium, and representing patient BALL01 as an example (Fig. 4B), we generated a ranked list of new pan-ALL targets, which included HSPB1, PARP1, and PRDX1 as top-ranked candidates (Fig. 4C). We selected to further characterize PARP1 as a candidate target since PARP1/2 inhibitors are already developmental therapeutics for a variety of pediatric tumors (13). Additionally, PARP1 is activated by DNA damage as a repair mechanism (14), and "cellular responses to DNA damage", showed enrichment in our prior pathway enrichment analysis, providing further confirmation that this pathway is overexpressed and stable (Fig. 3E). We sourced viably-frozen ALL samples (n=13) from the BCCH Biobank, including matched specimens used in our discovery cohort (n= 4), additional ALL specimens (n=13), and non-cancer pediatric stem cell samples (n=5), and treated these samples with graded doses of two PARP1/2 inhibitors, Olaparib and PJ34. Image-based drug screening of ALL cells co-cultured with MSC demonstrated high cytotoxic specificity of PARP1/2 inhibitors for ALL relative to non-cancer stem cell samples, as determined by IC50 values for each sample (Fig. 4D,E). The significant sensitivity of ALL cells to PARP1/2 inhibitors relative to non-cancer cells indicates that this may be a potential pan-ALL therapeutic target that was initially discovered through protein abundance analysis.

DISCUSSION

Molecularly guided targeted therapies have a high potential to improve outcomes for pediatric cancer patients. Yet, only 3-58% of patients receive molecularly guided therapies and even fewer report a positive response to treatment in NGS-guided trials (15). These unsatisfactory outcomes are likely the result of multiple limitations, including the reliance on genomics for target identification, which cannot capture plasticity of downstream transcriptional, translational and post-translational processes that impact target abundance and drug sensitivity, and the restricted enrollment for high-risk or relapsed cancers, which often progress quickly. Several initiatives, including ZERO and INFORM, have recently exemplified the use of precision oncology at diagnosis to help refine, or even change subtype diagnosis for several cancer types, which can lead to more appropriate treatment options (16,17). It is actively debated whether initiating molecular analyses for precision oncology at diagnosis is beneficial. Here, we advance the

medRxiv preprint doi: https://doi.org/10.1101/2022.03.04.22271927; this version posted March 8, 2022. The copyright holder for this preprint (which was not certified by peer review) is the author/funder, who has granted medRxiv a license to display the preprint in perpetuity. It is made available under a CC-BY-NC-ND 4.0 International license .

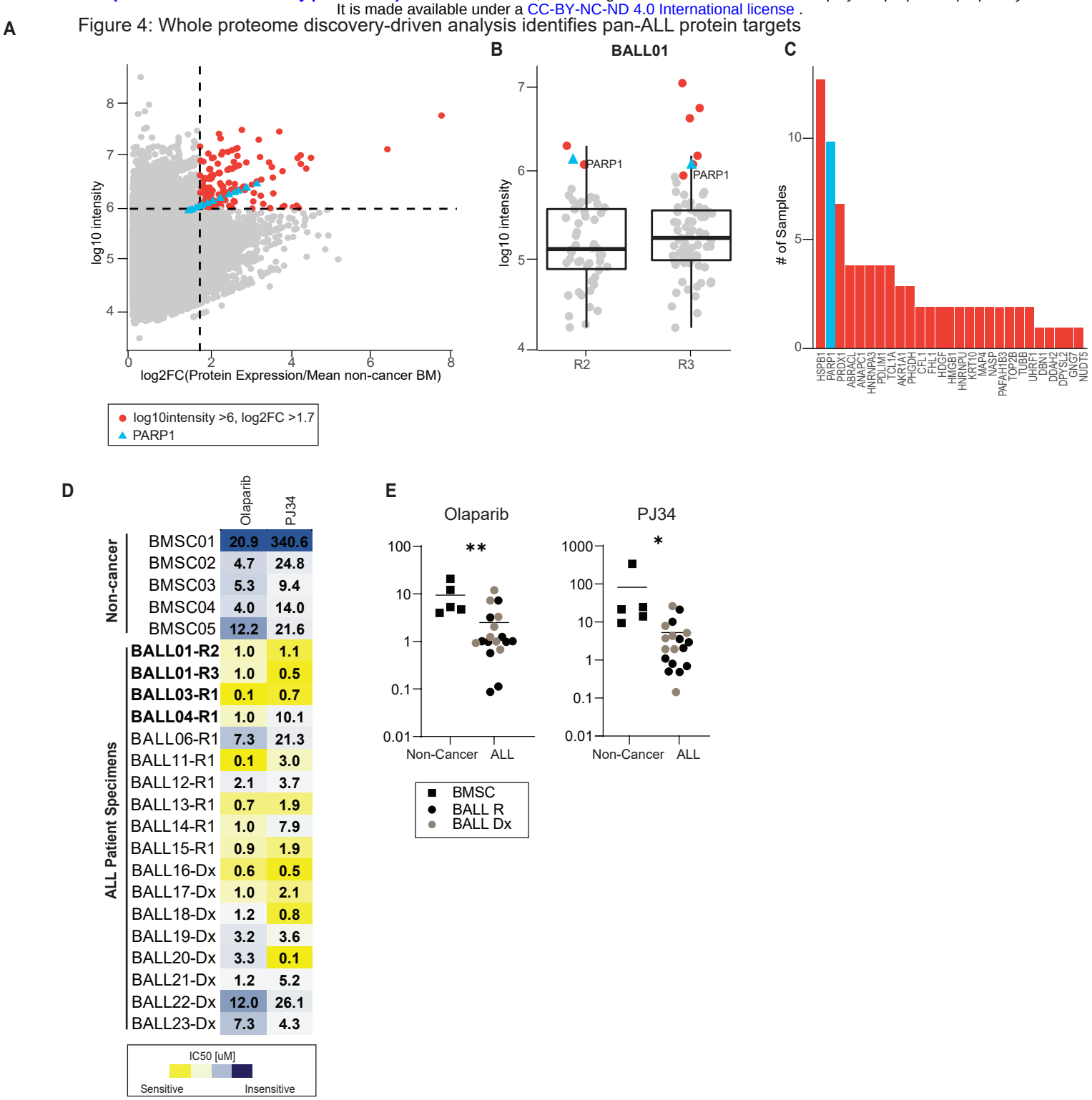

Figure 4: Whole proteome discovery-driven analysis identifies pan-ALL protein targets

A. Correlation of log2 fold-change (FC)/non-cancer vs protein expression (log10 intensity) for all proteins in all samples (filtered for proteins identified in at least ten of seventeen samples). Dashed lines represent cut-offs for top five percent of the population for each parameter. Proteins that meet both cut-offs are colored in orange and PARP expression is represented by blue triangles.

B. Representative figure (BALL01) showing all proteins that are >log2FC of 1.7. Only the proteins that have log10 intensity >6.0 (top 5%) are colored in orange.

C. Summary of all proteins of interest (proteins that pass all cut-offs) plotted by number of samples the protein meets the indicated parameters.

D. Measured IC50 values for Olaparib or PJ34 measured against ALL or non-cancer samples from patients treated at BCCH (n= 5 non-cancer, 8 diagnostic samples, 10 relapse samples). Samples were co-cultured with hTERT-MSCs and separately treated with the two PARP1/2 inhibitors. IC50 [μM] are colored by most sensitive in yellow to least sensitive in blue. Measurements represent the mean of n=2 replica wells from a single experiment. Bolded Patient IDs indicate patient samples analyzed in the pan-ALL target proteomic analysis.

E. Dot plots for IC50 [μM] values for Olaparib or PJ34 measured against non-cancer specimens (black square), primary diagnostic samples (light brown circle) or primary relapse samples (black circle). Measurements represent the mean of n=2 replica wells from a single experiment. Significance (*, **) is assigned by t-test p-value <0.01 and p-value <0.001 respectively.

medRxiv preprint doi: https://doi.org/10.1101/2022.03.04.22271927; this version posted March 8, 2022. The copyright holder for this preprint (which was not certified by peer review) is the author/funder, who has granted medRxiv a license to display the preprint in perpetuity. It is made available under a CC-BY-NC-ND 4.0 International license .

debate by contributing new evidence of high retention of druggable targets in pediatric ALL. We show that the stability extends to and may even be more pronounced at the protein level and that proteome analysis can inform target selection in addition to and independent of genomic analysis.

One challenge to initiating precision medicine at diagnosis is the prospect that the dominant relapse clones contain distinct mutations and unique drug sensitivities (3,18–20). While it is estimated that 37% of primary tumours retain druggable events at relapse (15), we show that a far higher fraction (64% of 80 patients) of primary ALL retain at least one druggable target. This high level of persistence was further reflected in the overall correlation of drug sensitivities between diagnosis and relapse. In our assay, genome variants predicted sensitivity to a targeted MEK inhibitor, which is consistent with prior studies (21,22). However, we found no correlation between the presence of *CDKN2A* deletion in primary ALL samples and sensitivity to CDK4/6 inhibition. Indeed, the utility of *CDKN2A* deletion to act as a predictive biomarker for sensitivity to CDK4/6 inhibitors is currently unresolved (23–26). Taken together, our data supports the notion that common genomic biomarkers are not sufficient to predict tumor sensitivity to variant-targeted monotherapies (27).

To supplement NGS-guided target identification, some precision oncology initiatives are complementing genome analysis with additional molecular strategies such as RNA-seq or Methyl-seq (15,16,28). Our study is among the first to conduct comprehensive targeted and non-targeted, paired Dx and Relapse proteome analyses of pediatric ALL. We found that tumour proteomes provide novel insights into disease biology and progression. For instance, targeted sequence analysis indicated considerable evolution in BALL03, but the CAP proteome analysis was highly stable ($r=0.78$ $p<4.1e-07$). Similarly, the relapse BALL04 sample gained a TP53 mutation, but CAP stability, proteome stability (equivalence of 90%), and drug responses were highly correlated with the diagnostic sample. Thus, evolution of minor clones through disease progression may not dramatically impact the expressed proteomes.

Proteomic analysis can also reveal new potential targets (29–31). Consistently, we identified PARP1, PRDX1 and HSPB1 as overexpressed pan-ALL target candidates. Moreover, we

medRxiv preprint doi: https://doi.org/10.1101/2022.03.04.22271927; this version posted March 8, 2022. The copyright holder for this preprint (which was not certified by peer review) is the author/funder, who has granted medRxiv a license to display the preprint in perpetuity. It is made available under a CC-BY-NC-ND 4.0 International license .

validated the sensitivity of B-ALL samples to PARP1/2 inhibition *in vitro*. These proteome-based pan-ALL targets may warrant further investigation of their actionability in pediatric ALL. However, we note the conclusions drawn from our proteome analyses and image-based drug screening are limited by the number of matched patient samples examined, the variety of genetic subytypes, and the ethnic diversity of the patients treated in our single site cohort. In addition, image-based drug screening of ex vivo ALL-MSC co-cultures may not accurately reflect responses in patients although it has been shown to capture leukemia-intrinsic differences in cell proliferation and survival and, in the case of venetoclax, ex vivo responses correlate with strong *in vivo* antileukemic activity (32). Finally, our retrospective design was useful for studying matched Dx-R samples, which are relatively rare and difficult to predict prospectively. With these potential caveats in mind, the findings from this study indicate the potential utility for prospective proteogenomic variant identification, initiating at disease diagnosis, for the targeted treatment of pediatric relapse ALL.

medRxiv preprint doi: https://doi.org/10.1101/2022.03.04.22271927; this version posted March 8, 2022. The copyright holder for this preprint (which was not certified by peer review) is the author/funder, who has granted medRxiv a license to display the preprint in perpetuity. It is made available under a CC-BY-NC-ND 4.0 International license .

ACKNOWLEDGEMENTS

This work was supported by the Michael Cuccione Foundation (MCF) and the BC Children's Hospital Foundation through the Better Responses through Avatars and Evidence (BRAVE) Initiative. Salary support was provided by the MCF (CJL, GSDR, CAM, PFL), the Canada Research Chairs Program (PFL), the Michael Smith Foundation for Health Research Scholar Program (PFL) and the University of British Columbia (AL, EKE).

Affiliations of authors: Department of Pediatrics, University of British Columbia, Vancouver, BC, Canada (AL, MG, NMA, CJL, GSDR, CAM); Michael Cuccione Childhood Cancer Research Program, BC Children's Hospital, Vancouver, BC, Canada (AL, MG, NMA, CJL, GSDR, PFL, CAM); Department of Pathology, University of British Columbia, Vancouver, BC, Canada (EKE, PFL).

We thank Pascal Leclair for contributions made through the BRAVE Initiative and technical assistance. We gratefully acknowledge the participation of the patients and families that made this study possible and the BC Children's Hospital nurses and physicians and Biobank staff for their tremendous efforts in collecting and maintaining specimens. We also acknowledge our consultations with the Modeling node and Proteomics node of the Terry Fox Precision Oncology for Young People Translational Research Program.

medRxiv preprint doi: https://doi.org/10.1101/2022.03.04.22271927; this version posted March 8, 2022. The copyright holder for this preprint (which was not certified by peer review) is the author/funder, who has granted medRxiv a license to display the preprint in perpetuity. It is made available under a CC-BY-NC-ND 4.0 International license.

Supplementary Figure 1: Genomic lesions detected in paired ALL specimens from the BCCH cohort

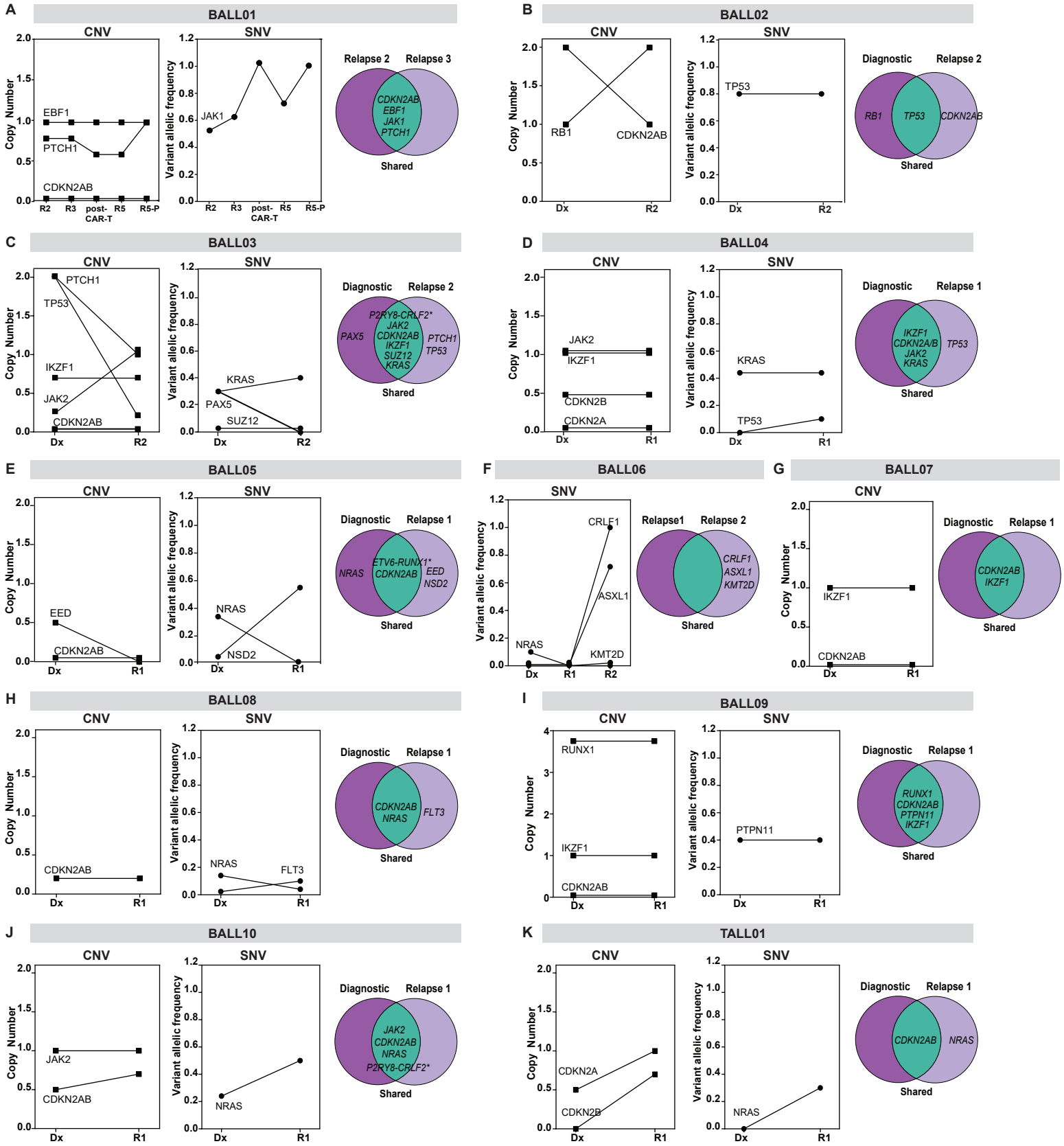

Supplementary Figure 1: Genomic lesions detected in paired ALL specimens from the BCCH cohort

A-K. Line graphs for each patient treated at BCCH represent genomic lesions identified through targeted NGS in samples collected through disease progression. Only abnormal variants are plotted. CNVs are plotted by the number of copies detected and SNVs are plotted by the allelic frequency. Venn diagrams for each patient display variants that are unique to diagnosis (Dx unique), unique to relapse (R unique), or shared between samples in a progression series. An asterisk indicates the lesion is a gene-fusion detected by RNA analysis.

medRxiv preprint doi: https://doi.org/10.1101/2022.03.04.22271927; this version posted March 8, 2022. The copyright holder for this preprint (which was not certified by peer review) is the author/funder, who has granted medRxiv a license to display the preprint in perpetuity. It is made available under a CC-BY-NC-ND 4.0 International license.

Supplementary Figure 2: Genomic lesions detected in paired ALL specimens from the SJH cohort

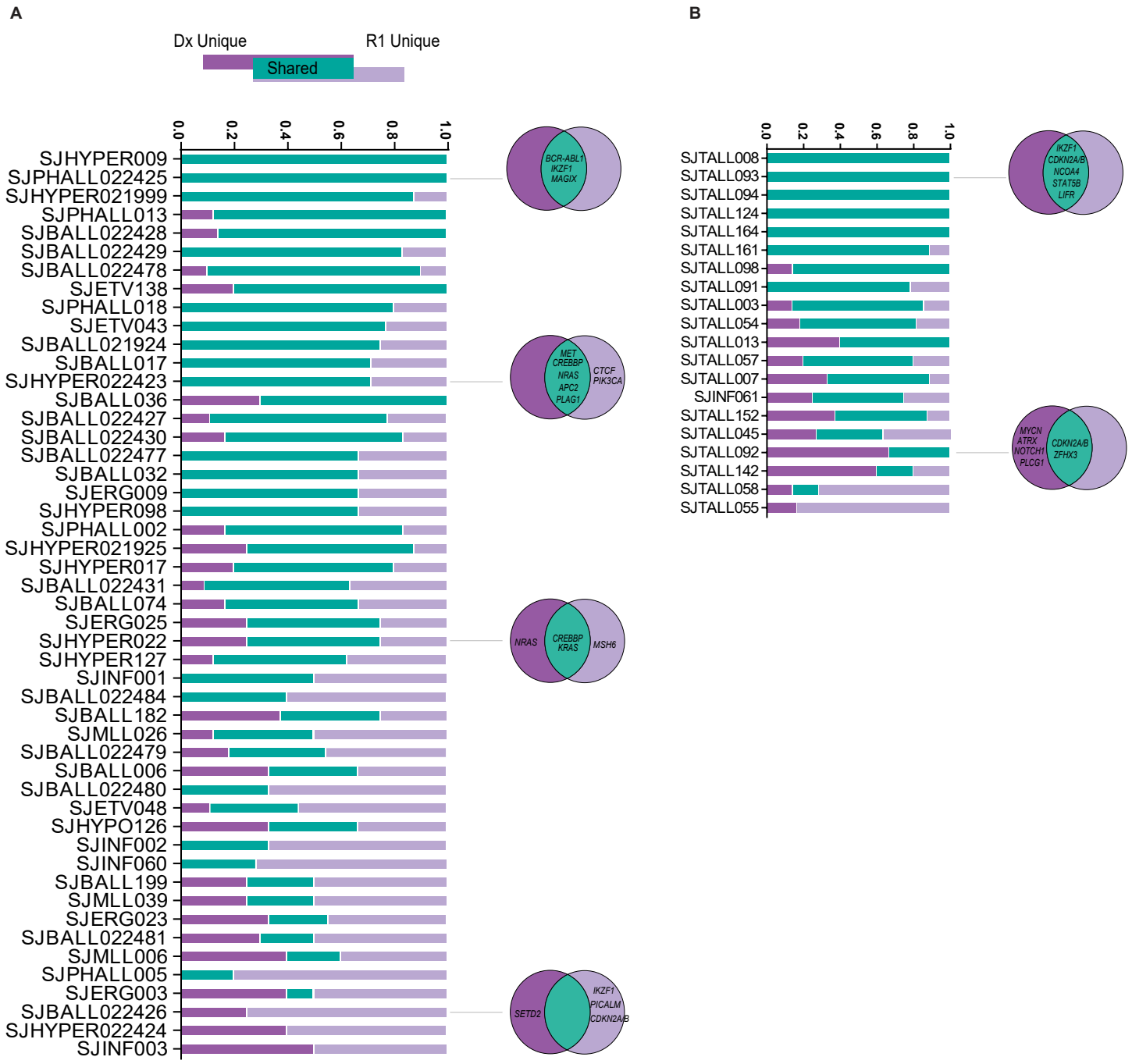

Supplementary Figure 2: Genomic lesions detected in paired ALL specimens from the SJH cohort

A. Bar graphs for each patient with B-ALL treated at SJH (n=49) illustrate the fraction of variants that are unique to diagnosis (Dx Unique, dark purple bars), unique to relapse (R unique, light purple bars), or shared (green bars), identified through whole genome sequencing in samples collected through disease progression. Venn diagrams are shown for selected patients to display the distribution of variants in a progression series.

B. Bar graphs for each patient with T-ALL treated at SJH (n=20) illustrate the fraction of variants that are unique to diagnosis (Dx Unique, dark purple bars), unique to relapse (R unique, light purple bars), or shared (green bars), identified through whole genome sequencing in samples collected through disease progression. Venn diagrams are shown for selected patients to display the distribution of variants in a progression series.

medRxiv preprint doi: https://doi.org/10.1101/2022.03.04.22271927; this version posted March 8, 2022. The copyright holder for this preprint (which was not certified by peer review) is the author/funder, who has granted medRxiv a license to display the preprint in perpetuity. It is made available under a CC-BY-NC-ND 4.0 International license .

Supplementary Figure 3: Dynamics of genomic lesions detected in the SJH and BCCH cohorts

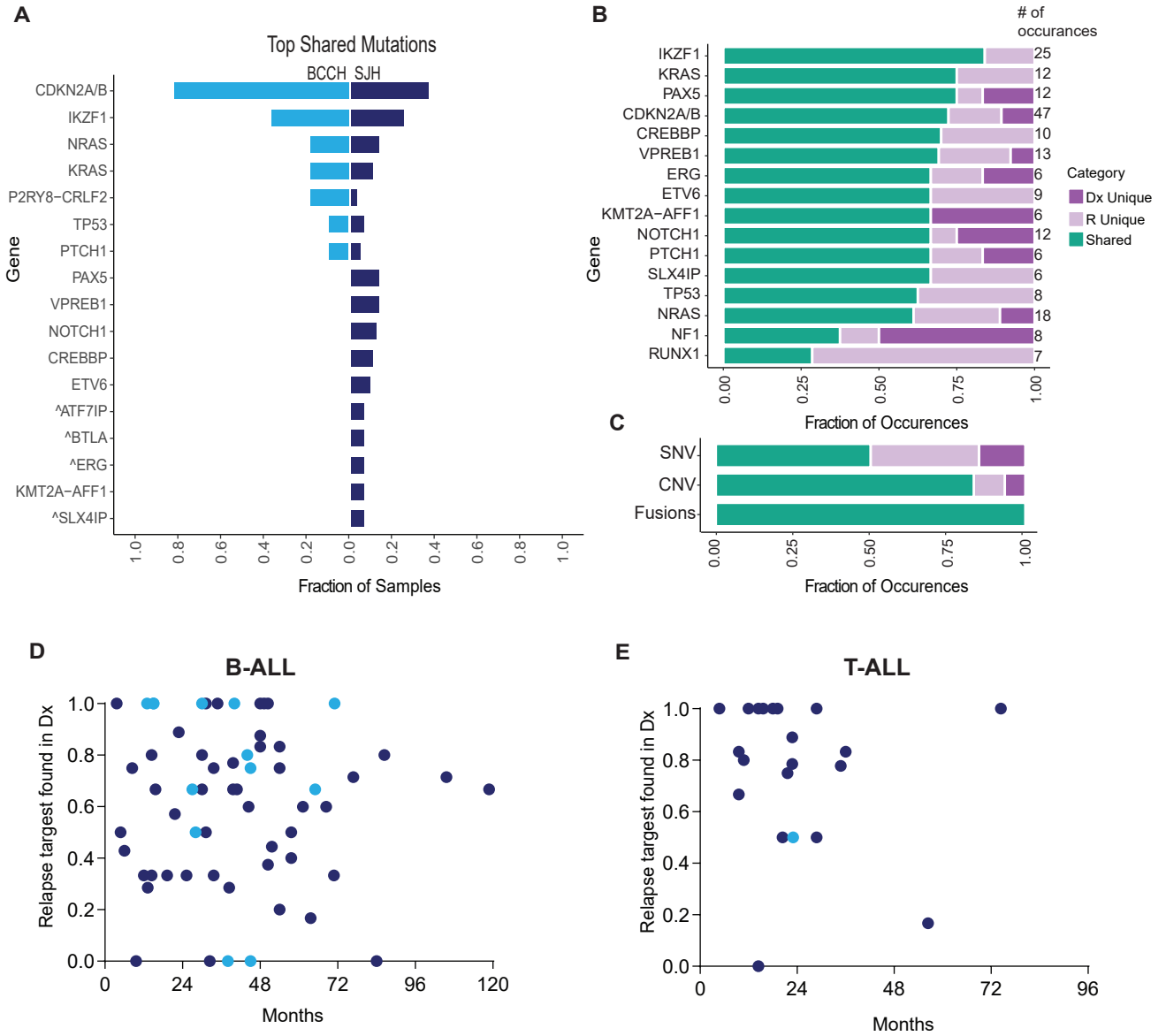

Supplementary Figure 3: Dynamics of genomic lesions detected in the SJH and BCCH cohorts

A. Bar plot for the most frequent variants (top 17) detected in both Dx and paired R samples (shared) plotted as the fraction of samples containing the shared variant in each cohort (n=11 from BCCH, n=69 from SJH). Variants were detected in the BCCH cohort through targeted NGS while variants were detected in the SJH cohort through whole genome sequencing. Thus, variants that cannot be detected in the BCCH samples with the targeting sequencing assay are indicated with ^.

B. Bar plot for the most prevalent genes (top 16) detected in the combined BCCH and SJH cohorts. Variants are categorized as shared (green), Dx unique (dark purple) or R unique (light purple) and plotted as the fraction of occurrences. The total number of times the gene was identified is displayed on the right end of the bar.

C. Bar plot classifying variants (SNV, CNV, Fusion) as shared (green), Dx unique (dark purple) or R unique (light purple) and plotted as the fraction of occurrence in the BCCH cohort.

D. Dot plot for fraction of shared variants versus time to relapse for 59 B-ALL patients (n= 10 from BCCH represented by light blue circle, n= 49 from SJH represented by dark blue circles).

E. Dot plot for fraction of shared variants versus time to relapse for 21 T-ALL patients (n= 1 from BCCH represented by light blue circle, n= 20 from SJH represented by dark blue circles).

medRxiv preprint doi: https://doi.org/10.1101/2022.03.04.22271927; this version posted March 8, 2022. The copyright holder for this preprint (which was not certified by peer review) is the author/funder, who has granted medRxiv a license to display the preprint in perpetuity. It is made available under a CC-BY-NC-ND 4.0 International license .

Supplementary Figure 4: Description of proteomic data filtering pipeline and quality assessment

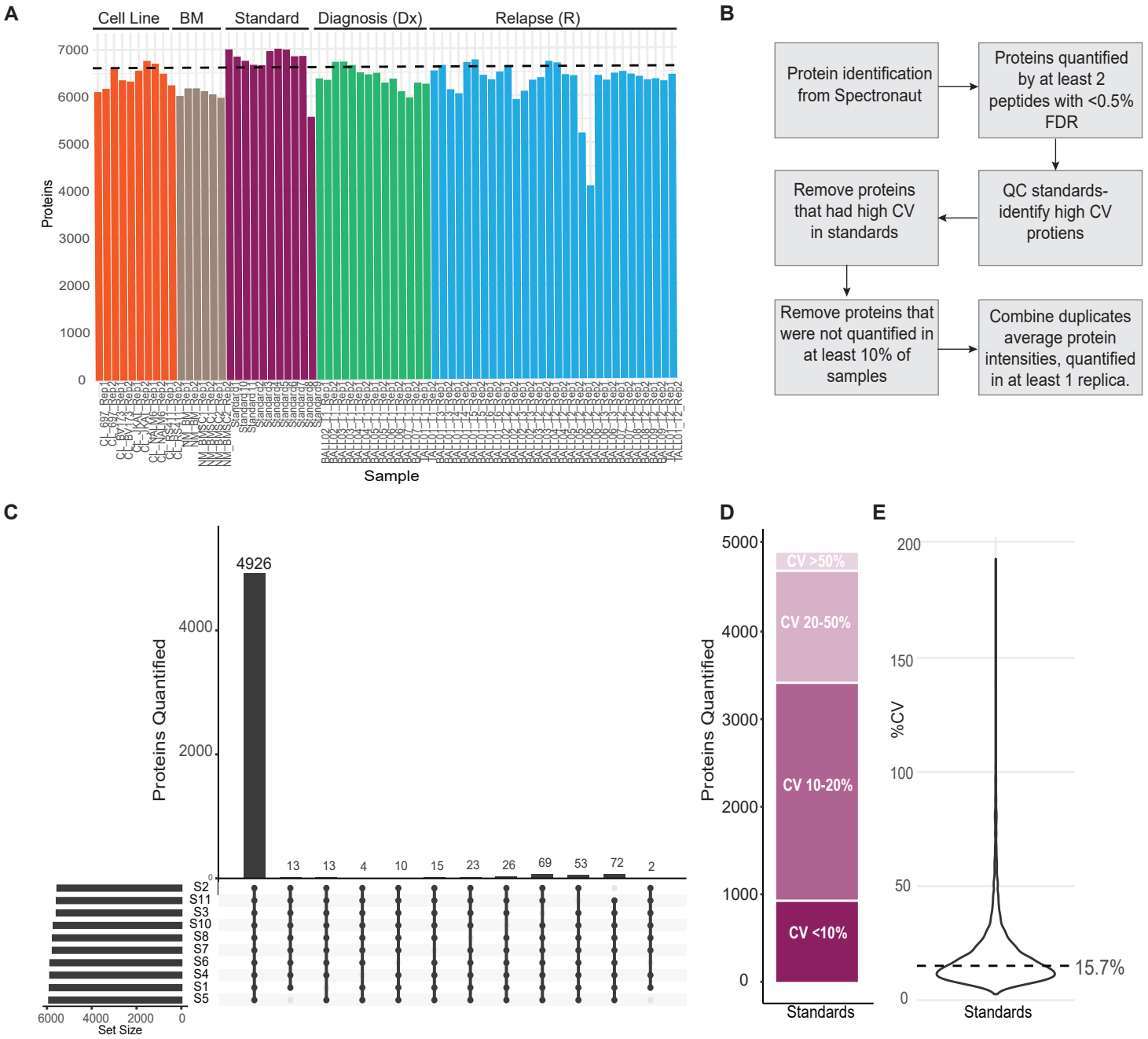

Supplementary Figure 4: Description of proteomic data filtering pipeline and quality assessment

A. Total proteins identified in each sample, prior to any filtering. The category of the sample type is listed across the top of each group.

B. Diagram of the filtering workflow to attain the final proteomics dataset utilized for subsequent analyses.

C. Upset plot for ten of the eleven standards (standard nine was removed due to a clear technical issue). Numbers reported are based on proteins quantified by a minimum of two peptides at a precursor q-value threshold of 0.5% FDR.

D. The cv for protein quantity across the ten standards was assessed and plotted by percent coefficient of variation (CV). The darkest purple bar at the bottom represents the number of proteins with a CV of less than 10% and so on, with the lightest bar at the top representing the number of proteins with a cv greater than 50%. This fraction of proteins with cv >50% was removed from the remaining data with the assumption these are unstably quantified between samples.

E. A violon plot demonstrating the median CV of protein quantification across the ten standards (including those >50% CV). Dashed line indicates the median CV (15.7%).

medRxiv preprint doi: https://doi.org/10.1101/2022.03.04.22271927; this version posted March 8, 2022. The copyright holder for this preprint (which was not certified by peer review) is the author/funder, who has granted medRxiv a license to display the preprint in perpetuity. It is made available under a CC-BY-NC-ND 4.0 International license .

Supplementary Figure 5: Evaluation of individual sample data quality

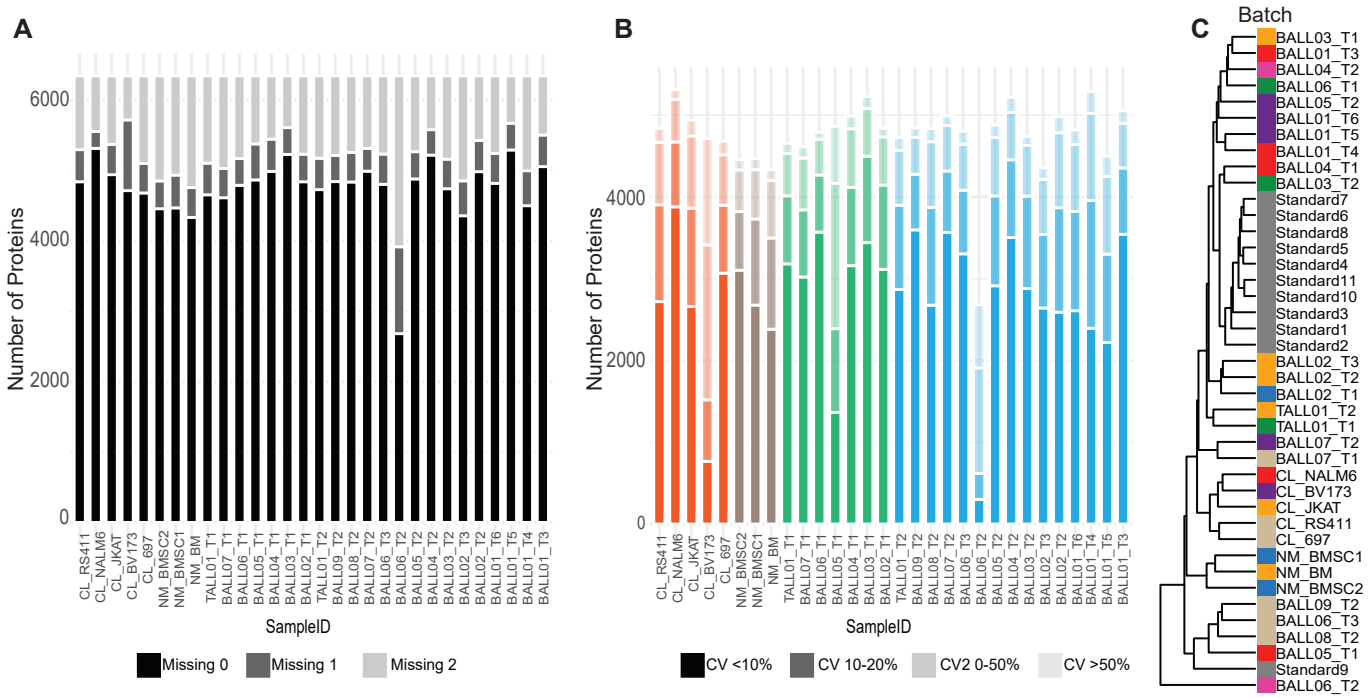

Supplementary Figure 5: Evaluation of individual sample data quality

A. Bar plot to demonstrate data completeness between replica of each sample. Proteins that were identified in both replica are represented in black, dark grey represents proteins that were only identified in one of the replica, and light grey represents proteins that were entirely missing from the pair.

B. CV between replica is represented as described in panel S5 D; The darkest color bar at the bottom represents the number of proteins with a CV of less than 10% and so on, with the lightest bar at the top representing the number of proteins with a cv greater than 50%.

C. Unsupervised hierarchical clustering was performed to evaluate any bias due to batch effects. Colors represent batches. The standards are represented in grey, as these were a mix of samples from different batches.

medRxiv preprint doi: https://doi.org/10.1101/2022.03.04.22271927; this version posted March 8, 2022. The copyright holder for this preprint (which was not certified by peer review) is the author/funder, who has granted medRxiv a license to display the preprint in perpetuity. It is made available under a CC-BY-NC-ND 4.0 International license .

Supplementary Figure 6: Significant cancer associated proteins (CAPs)

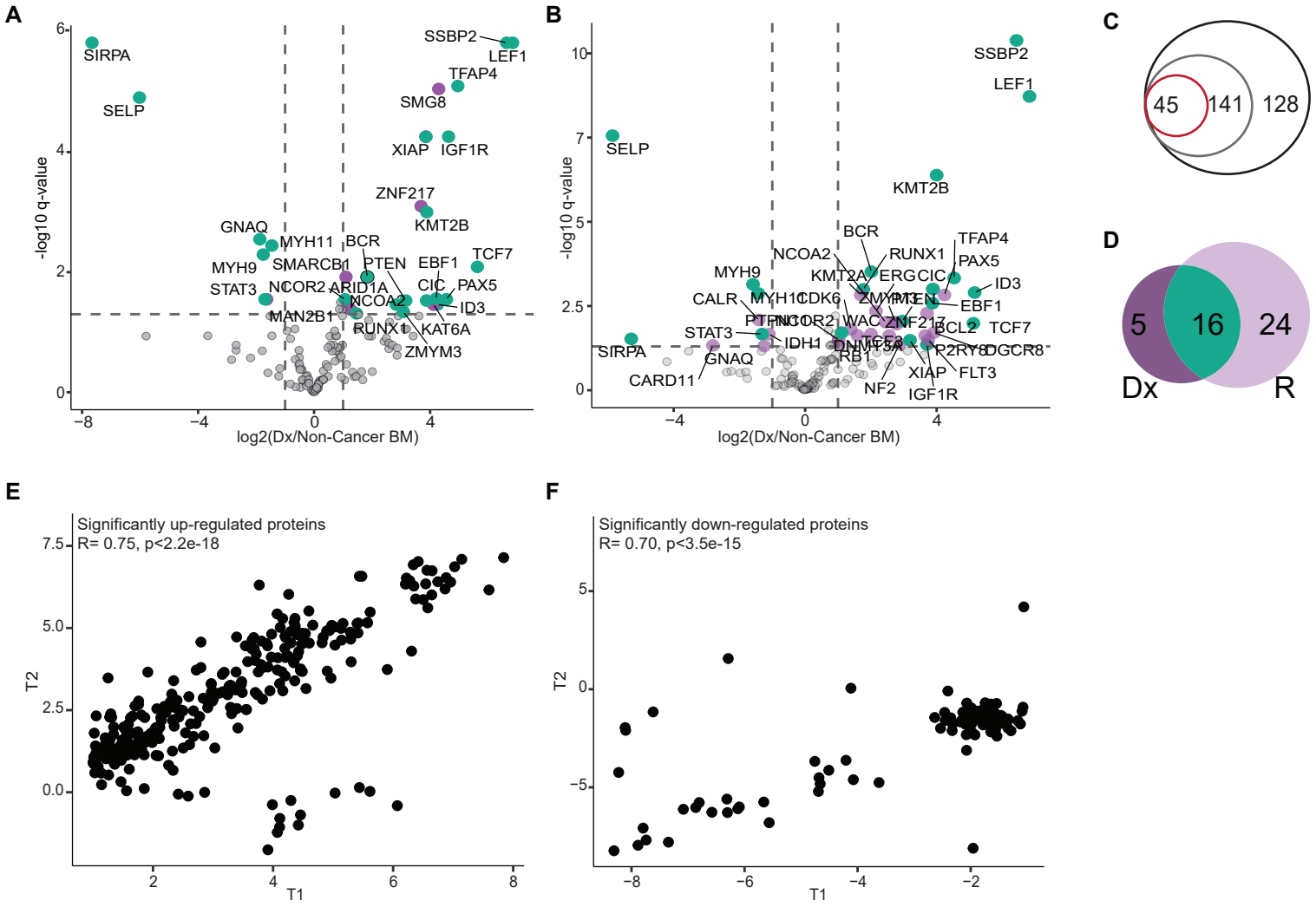

Supplementary Figure 6: Significant cancer associated proteins (CAPs)

A. 141 proteins were tested using LIMMA (log2FC>1, p-value adjusted FDR<0.05); Initial Diagnosis (Dx) samples vs. Non-cancer BM samples on the left and Relapse (R) vs Non-cancer BM samples on the right. Proteins that are significantly over expressed in both Dx and R are colored in green and those that are unique to either Dx or R are colored in purple.

B. From the list of 269 pediatric cancer driving proteins (black circle), 141 proteins were detected in our data (gray circle) and 45 proteins were deemed significant (red circle).

C. Sixteen of the overexpressed proteins were shared between Dx and R (bottom)

D. Of the 45 proteins that were overexpressed at Dx, the protein expression for each protein at each timepoint was plotted as timepoint 1 (T1) vs timepoint 2 (T2) (calculated as the log2(protein expression/the average protein expression in the non-cancer bone marrow (BM) samples). A Pearson's r correlation was calculated for the entire dataset.

E. Of the 45 proteins that were under-expressed at Dx, the protein expression for each protein at each timepoint was plotted as timepoint 1 (T1) vs timepoint 2 (T2) (calculated as the log2(protein expression/the average protein expression in the non-cancer bone marrow (BM samples). A Pearson's r correlation was calculated for the entire dataset.

medRxiv preprint doi: https://doi.org/10.1101/2022.03.04.22271927; this version posted March 8, 2022. The copyright holder for this preprint (which was not certified by peer review) is the author/funder, who has granted medRxiv a license to display the preprint in perpetuity. It is made available under a CC-BY-NC-ND 4.0 International license .

Supplementary Figure 7: Statistical analysis of paired samples

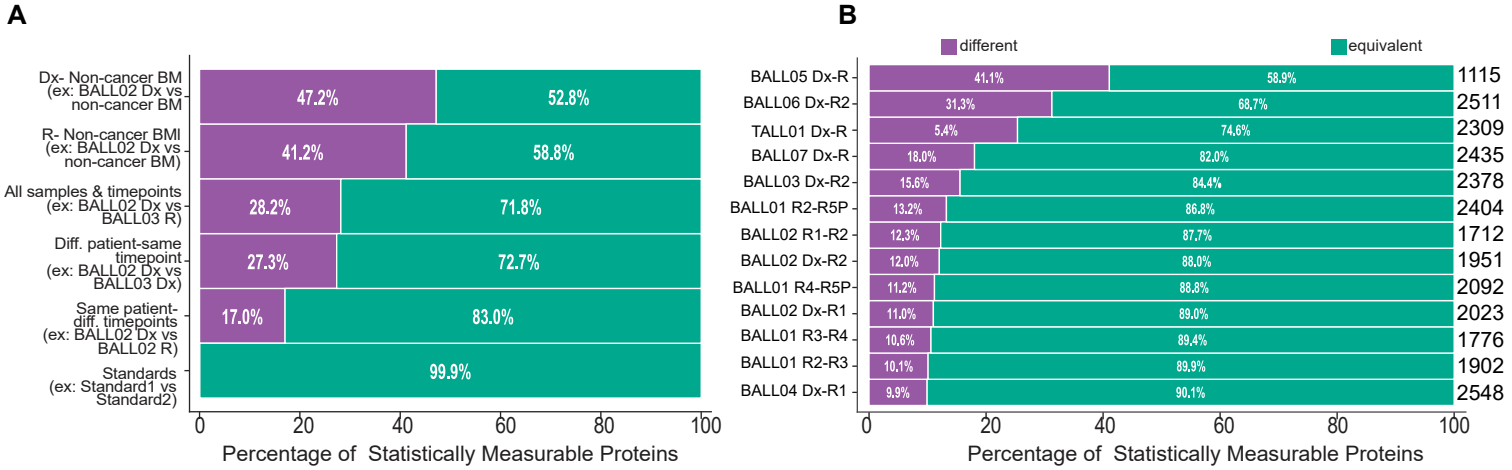

Supplementary Figure 7: Statistical analysis of paired samples

A. Summary of tests for differential expression and equivalence between different groups and pairings. Proteins that are statistically equivalent are represented in green (Two-one-sided t-test (TOST) for equivalence, boundaries between log2FC<-1 and log2FC>1), proteins that are statistically different are represented in purple (student's ttest p-value<0.05, log2FC>1. The bar represents the mean equivalence or difference of all protein expression for each pairing within the group.

B. Similar representation for each individual patient pairing of the group "Same patient-diff timepoints" group. The numbers on the right of each bar indicate how many statistically measurable proteins were in each pairing.

medRxiv preprint doi: https://doi.org/10.1101/2022.03.04.22271927; this version posted March 8, 2022. The copyright holder for this preprint (which was not certified by peer review) is the author/funder, who has granted medRxiv a license to display the preprint in perpetuity. It is made available under a CC-BY-NC-ND 4.0 International license .

MATERIALS AND METHODS

Patient samples & non-cancer controls. Patient specimens were collected by Biobank staff at BC Children's Hospital. Samples were taken with informed consent during routine clinical care. Sample collection and experiments were performed as approved by the University of British Columbia Children & Women's Research Ethics, and conformed with standards defined in the WMA Department of Helsinki and the Department of Health and Human Services Belmont Report.

Mononuclear cells containing leukemic blasts were isolated by Ficoll-Paque PLUS density centrifugation, viably frozen and preserved. Aliquots of patient samples, and patient clinical information were de-identified prior to release for this study. Leukemia samples were immunophenotyped at the clinical hematopathology laboratory using established ALL subtype-specific 10-colour flow cytometry panels according to clinical standard operating procedures. Patient bone marrow morphology was assessed by hematopathologists and cytogenetics studies were performed by clinical cytogeneticists. Upon receipt of the specimens, patient mononuclear cells were thawed at 37°C for 1-2 minutes, washed 1x in warm RPMI-1640 medium containing 10% fetal bovine serum (FBS, Invitrogen, Waltham, Massachusetts, USA) and washed 2x with PBS and stored as 5X10^5 – 1X10^6 cells per cell pellet.

Bone marrow stem cells (BMSC) from five non-cancer individuals were initially collected following routine procedures for bone marrow stem cell transplantation, and remaining material was stored viably with the BCCH Biobank. In addition, we obtained bone marrow mononuclear cells from one healthy individual (non-cancer BM). Finally, for analysis of mature B-cells, PBMCs from five patients that did not have any hematological malignancies that were in a similar age range were combined.

DNA/RNA extraction and sequencing. DNA and RNA extraction were performed using an Allprep (Qiagen) workflow. Library preparation and targeted sequencing was performed using the Oncomine Childhood Cancer Research Assay (OCCRA) on an Ion Chef and Ion Torrent S5 platforms (Thermo Fisher Scientific) following the manufacturer's protocols. OCCRA comprises

medRxiv preprint doi: https://doi.org/10.1101/2022.03.04.22271927; this version posted March 8, 2022. The copyright holder for this preprint (which was not certified by peer review) is the author/funder, who has granted medRxiv a license to display the preprint in perpetuity. It is made available under a CC-BY-NC-ND 4.0 International license .

2,031 unique DNA-based amplicons to detect SNVs, and CNVs, and 1,701 RNA-based amplicons to detect unique fusion or structural variants (9). The average read depth for the OCCRA panel was 5×10^6 – 7×10^6 per sample for DNA and 1x10^6 - 2x10^6 for RNA. SNVs were retrieved with Ion Reporter software (version 5.2). Copy number measurements were retrieved with Ion Reporter software (version 5.2) for genes with >5 probes, including those that were validated for copy number gains as described elsewhere (9).

St. Jude's Hospital (SJH) data curation. Data was downloaded from www.stjuderesearch.org/site/data/relapsed-all in December 2018. For our analysis, we included patients with Dx-R1 progression. To determine gene mutations as Dx unique, Shared, of Relapse unique, we included genes listed as "rise" as a shared mutation and genes listed as "fall" as Dx unique (Supplementary Table S3).

Cytotoxicity analysis of variant-predicted drug response in paired Dx-R ALL samples. hTERT-immortalized mesenchymal stromal cells (MSCs) were provided by D. Campana (St. Jude's Hospital). hTERT-MSCs were seeded at 5,000 cells per well in 200 µL of RPMI-1640 medium containing 10% fetal bovine serum (FBS, Invitrogen) and 1µM hydrocortisone (Sigma) in a 96-well plate (Corning, Corning, New York, USA), 24 hours prior to seeding with primary B-ALL or non-cancer bone marrow stem cells. Primary samples were thawed at 37°C for 1-2 minutes, washed 1x in warm RPMI-1640 medium containing 10% FBS and washed 2x with PBS, and stained with DAPI CFSE stain (Invitrogen) used to distinguish the ALL cells from the hTERT-MSC cells. The media was removed before adding 5x10^4 B-ALL cells in 100 µL of AIM-V medium (Thermo-Fisher).

Drug dilutions were prepared at 2x the final concentration (1nM, 10nM, 100nM, 1VM, 20µM, and 30µM) and 100µl of each drug dilution was added to 100µl of primary cells in each well. Cells were incubated with the drugs for 72 hours at 37°C in a 5% (v/v) CO2 incubator. Drugs used in the study: Palbociclib, Trametinib, Ruxolitinib, and Vismodegib (Selleck Chemicals LLC, Houston, TX, USA). For PARP1/2 inhibitors, the drugs were prepared for final concentrations of 1nm to 100µM in 10-fold increments PJ34 (SelleckChem), 0.1nM to 10µM in 10-fold increments for Olaparib (SelleckChem).

medRxiv preprint doi: https://doi.org/10.1101/2022.03.04.22271927; this version posted March 8, 2022. The copyright holder for this preprint (which was not certified by peer review) is the author/funder, who has granted medRxiv a license to display the preprint in perpetuity. It is made available under a CC-BY-NC-ND 4.0 International license .

After 72 hours, GFP viability dye was added and incubated at room temperature for 1 hour. The plate was analyzed by a high content image analysis system (ImageXpress Micro XL). Images were taken using a 40X 0.75 NA dry objective with the MetaXpress 5.0.2.0 software (Molecular Devices Inc) on the ImageXpress Micro XL epifluorescence microscope (Molecular Devices Inc). DAPI and GFP (green fluorescent protein) emissions were acquired simultaneously with a 505DCXR beam splitter (Dual-View; Optical Insights, LLC) with the optical filters for DAPI excitation or GFP emission, respectively. For the analysis of the proportion of living cells, images were taken once per site using 50-ms exposures, 2x2 binned resolution, with 100% of full lamp intensity for each channel, and 25 optical sections spaced 500 µm apart. Post-acquisition processing of images was performed using MetaXpress offline.

Viability was calculated by taking the mean of (DAPI and GFP double-positive (DP) cells)/ (DAPI single-positive cells) for each drug-treated well. To account for relative viability of the primary cells in the assay, the drug-treated viability was normalized to the calculated viability for the vehicle-treated (DMSO) cells. For PARP1/2 inhibitors, normalized viability was assessed by the summation of DP cells across four sites in drug-treated wells / summation of DP cells across 4 sites in DMSO-treated wells. IC50 concentrations were calculated in GraphPad PRISM version 9 (GraphPad Software, San Diego, CA, USA) with the method "log inhibitor concentration vs normalized response".

Protein extraction and LC-MS/MS acquisition. Unless otherwise stated, reagents were purchased from Sigma Aldrich (St. Louis, Missouri, United States). Pellets of 5X10^5 – 1X10^6 cells were lysed in 50µl buffer containing 1% SDS (Fisher BioReagents, Pittsburgh, Pennsylvania, United States), 1X Pierce protease inhibitor (Thermo Fisher Scientific) in 50 mM HEPES (pH 8.0), followed by 5 minute incubation at 95 °C and 5 minutes on ice. The sample was incubated with benzonase (EMD Millipore/Novagen, Massachusetts, USA) at 37 °C for 30 minutes to shear chromatin. Following benzonase treatment, each sample was reduced with 10mM Dithiothreitol (DTT) dissolved in 50mM HEPES pH 8.0 (37°C, 30 minutes) and alkylated with 40 mM Chloroacetamide (CAA) dissolved in 50mM HEPES pH 8.0 (30 minutes in the dark) and quenched in 40 mM DTT for 5 minutes at room temperature.

medRxiv preprint doi: https://doi.org/10.1101/2022.03.04.22271927; this version posted March 8, 2022. The copyright holder for this preprint (which was not certified by peer review) is the author/funder, who has granted medRxiv a license to display the preprint in perpetuity. It is made available under a CC-BY-NC-ND 4.0 International license .

Lysates were cleaned using single-pot solid-phase-enhanced (SP3) bead technique (33) using hydrophilic and hydrophobic Sera-Mag Speed Beads (GE Life Sciences, Issaquah, Washington, United States). Proteins were bound to paramagnetic beads with 100% ethanol (80% v/v), incubated for 18 minutes at room temperature, and washed twice with 90% ethanol using magnetic isolation. Beads were then resuspended in 30µl 200 mM HEPES, pH 8.0, and incubated with sequencing-grade trypsin (Promega Madison, Wisconsin, United States) at 1:50 protein ratio for sixteen hours at 37 °C, and afterwards acidified to pH 3-4 with formic acid. Peptide digests were de-salted on Nest Group Inc. C18 spin columns with 0.1% trifluoroacetic acid (TFA), eluted with 60% acetonitrile in 0.1% FA and dried in a vacuum concentrator. Dried samples were resuspended in 0.1% formic acid (FA).

Library Preparation- Gas Phase Fractionation. Online gas-phase fractionation was performed. 1-2 µg de-salted peptides from select samples were combined into a single pool and analyzed in ten fractions, 1 µg per fraction. The first eight fractions (340 m/z to 760 m/z) were analyzed over a 60 m/z window (ie 340 m/z – 400 m/z is fraction 1) each with a loop count of 30 and window size of 2 m/z. The final two fractions (820 m/z-1180 m/z) were analyzed over 180 m/z window each, with a loop count of 30 and 6 m/z window.

Peptides were separated on a PharmaFluidics 50cm uPAC™ (ESI Source Solutions, Woburn, MA, United States), maintained at 50 °C on an Easy-nLC 1200 connected to a Q Exactive HF mass spectrometer (Thermo Fisher Scientific). The peptides were separated over a 3 hour gradient consisting of Buffer A (0.1% FA in 2% acetonitrile) and 2% to 80% Buffer B (0.1% FA in 95% acetonitrile) at 300 nL/min. MS acquisition consisted of a MS1 scan ranges specified above for each fraction (AGC target of 3e6 or 60 ms injection time), and resolution of 120,000. DIA segment spectra were acquired with a AGC target 3e6, resolution 30,000, auto ms injection time, and stepped collision energy of 25.5, 27, 30. The library was also supplemented with DIA data from each individual sample.

Patient Sample MS acquisition. 1 µg of peptides was injected for analysis for each sample. Samples were randomized and we obtained duplicate injections. We created a representative

medRxiv preprint doi: https://doi.org/10.1101/2022.03.04.22271927; this version posted March 8, 2022. The copyright holder for this preprint (which was not certified by peer review) is the author/funder, who has granted medRxiv a license to display the preprint in perpetuity. It is made available under a CC-BY-NC-ND 4.0 International license .

pool of 15 ALL primary and cell line samples to be injected approximately every 10 samples for quality control, referred to as "standard". The DIA method consisted of a MS1 scan from 300 to 1650 m/z (AGC target of 3e6 or 60 ms injection time), and resolution of 120,000. DIA segment spectra were acquired with a twenty-four-variable window format, (AGC target 3e6, resolution 30,000, auto for injection time), and stepped collision energy of 25.5, 27, 30. We added indexed retention time (iRT) peptides (Biognosys, Schlieren, Switzerland) to each sample for retention time normalization and quality control.

Proteomics Data Analysis. For a summary of data quality and filtering, refer to Supplementary Fig. S4, S5. Briefly, the raw DIA files were analyzed with Spectronaut Pulsar X (Biognosys, Schlieren, Switzerland) using a human FASTA file from UniProt (reviewed 20200309). This FASTA file includes common contaminants. Additionally, a FASTA file for iRT peptides, provided by Biognosys, was included in the search. Search was performed using the factory settings including specificity for Trypsin, Carbamidomethyl (C) as a fixed modification, and Acetyl (protein N-term) and Oxidation (M) as variable modifications. Precursor, and protein identifications false discovery rate (FDR) threshold was set to 1%, while the threshold for peptide was 0.5%. A minimum of 2 peptides were required for quantitation. Protein intensities were normalized in Spectronaut using the "global" setting, which normalizes by median protein intensity per sample. Duplicate injections were averaged (mean). Proteins that were quantified with >50% CV in the 10 standards were removed from all samples as they are presumed to be un-reliably quantified. Furthermore, proteins identified in <10% of the samples were removed. Finally, missing values were imputed using a "down-shifted normal" imputation strategy. Briefly, a normal distribution was created out of the overall sample distribution, then shifted to lower values using magnitude of 3.5.

To summarize, we identified a total of 8153 unique proteins with an average of 6600 proteins per sample using a data independent acquisition approach (DIA) with a spectral library of 8183 proteins derived from gas-phase fractionated sample pool (Supplementary Fig. S4A). After quality assessment and data filtering (Supplementary Fig. S4B), we quantified an average of 5100 proteins per sample with at least 2 peptides at less than 0.05% FDR.

medRxiv preprint doi: https://doi.org/10.1101/2022.03.04.22271927; this version posted March 8, 2022. The copyright holder for this preprint (which was not certified by peer review) is the author/funder, who has granted medRxiv a license to display the preprint in perpetuity. It is made available under a CC-BY-NC-ND 4.0 International license .

Identification of cancer-associated proteins. Proteins were selected from two large-scale pediatric cancer studies that identified commonly mutated genes, genes of prognostic importance, and potential cancer drivers (9,10) (Supplementary Table S6). Additionally, targets were included from the OCCRA panel, which is similar to the Oncomine panels used in NCI-COG Pediatric MATCH precision medicine trial (21) (Supplementary Table S6).

For statistical analysis, the "Limma" package for R was used. P-value was adjusted using the Benjamin-Hochberg and the FDR threshold was 5%. Circos plots were created in R using the package "Circularize"; data was first filtered for proteins that were overexpressed relative to the non-cancer controls. Pearson correlation coefficient was calculated for each pairing based on proteins that were overexpressed in Dx.

Fluorescence-activated cell sorting to isolate mature B-cells. To investigate comparison to B-cells, we included data from naïve and memory B-cells isolated by flow cytometry from age-matched PBMCs. To decrease processing and patient-specific variability and increase sorting efficiency, we combined PBMCs from five patients that did not have any hematological malignancies and were in a similar age range (see Supplementary Table S1). Briefly, we thawed 1 vial (approximately 5X10^6 – 10X10^6 cells per vial) and washed once with sterile FACS buffer (PBS (Thermo Fisher Scientific) + 2% FBS (Thermo Fisher Scientific)). We used 25X10^6 live cells for staining. Cells were pelleted and resuspended in approximately 100 µl of FACs buffer. We utilized a previously established 8-color flow panel designed to identify CD45+ lymphocytes and then optimally separate T-cells and B-cells and their respective subpopulations; for this experiment we aimed to isolate two different mature B-cell populations, naïve B-cells (CD45+CD3-CD19+CD10-CD20+CD27-). and memory B-cells (CD45+CD3-CD19+CD10-CD20+CD27+). The panel consists of CD45-AF488(HI30), CD3-BV510(UCHT1), CD19-APCFire(HIB19), CD4-AlexaFluor700(SK3), CD8-PECy7(RPA-T8), CD10-BV421(HI10a), CD20-APC(2H7), CD27-PE(O323) (BioLegend). We added BV staining cocktail for optimal performance of the BV dye and human FC blocker to reduce unspecific binding. Staining was performed for 20 minutes at 4 °C in the dark. After staining, the cells were washed with FACS buffer, centrifuged at 1500 rpm and resuspended in 1 mL of FACS buffer.

medRxiv preprint doi: https://doi.org/10.1101/2022.03.04.22271927; this version posted March 8, 2022. The copyright holder for this preprint (which was not certified by peer review) is the author/funder, who has granted medRxiv a license to display the preprint in perpetuity. It is made available under a CC-BY-NC-ND 4.0 International license .

Just prior to sorting, we added 7AAD for viability. Sorting was done at the Center for Molecular Medicine and Therapeutics (CMMT) flow sorting core at BCCHR on an Astrios FACS sorter.

Statistical Analysis. To look at protein stability, we established a hybrid method that compares robustly quantified proteins using equivalence and differential expression testing. We normalized the quantitative protein data using median centring and standard samples 1,2,3, and 9 were removed. To create a robust comparison between statistically different and equivalent proteins for a given pair of samples, we employed coefficient of variation (CV) based filtration to filter out proteins with unstable quantification. Proteins with >20% CV between the technical replica for each sample were removed. Only proteins that passed this threshold in each-pairwise comparison remained, therefore there were no missing values or imputed data. The statistical tests were done on each pair of sample comparisons with their two technical replicates. The differential expression testing was done using a ttest_ind function from the stats package. Proteins resulting with p-value < 0.05 and logFC > 1 were designated as statistically different. The equivalence testing was done using the TOST two_raw function from the TOSTER package setting logFC<-1 and logFC>1 as boundaries for equivalence.

To obtain a list of equivalent proteins for gene ontology enrichment, we first ensured the protein was equivalent in at least two of the seven Dx-R pairings. We next removed the proteins attributed to "housekeeping" functions by creating a cancer vs. non-cancer pairings equivalent list, which also required the protein was detected in at least two pairings. Housekeeping proteins were then removed from our paired Dx-R equivalence list. To obtain the "difference" list, we similarly required "difference" in protein expression in at least two of the seven Dx-R (or R-R) pairings. To determine if the protein was Dx or R enriched, we first summed the FC across the pairings and if the total FC was below -1 it was considered R enriched, above +1 was considered Dx enriched and in-between was counted for both Dx and R, leading to two lists for analysis (Dx+ both and R+both).

For gene ontology analysis we used g:Profiler (BIIT! Research Group, g:Profiler version e104_eg51_p15_3922dba, database updated on 07/05/2021) with an FDR threshold of 5%. To attain better resolution of the pathway visualization, we followed a similar strategy previously

medRxiv preprint doi: https://doi.org/10.1101/2022.03.04.22271927; this version posted March 8, 2022. The copyright holder for this preprint (which was not certified by peer review) is the author/funder, who has granted medRxiv a license to display the preprint in perpetuity. It is made available under a CC-BY-NC-ND 4.0 International license .

described (34); we limited the terms to GO: Biological Process (BP) and limited the number of intersections to 1000. For visualization of the enriched terms, we employed Cytoscape (35) (version 3.8.2) and utilized the "EnrichmentMap" and "AutoAnnotate" packages. For TF enrichment, we created a list of equivalent proteins as previously described. However, these proteins had to be identified in at least three of the paired samples, and at least three of the cancer vs. non-cancer pairings. The enrichment was obtained from gProfiler, as described above. The background list for all GO analyses was a list of all proteins quantified in the data set.

Data Availability. MS data have been deposited to the Proteome Consortium (http://www.proteomexchange.org) via the MassiVE (https://massive.ucsd.edu/) partner repository data set MSV00008897.

medRxiv preprint doi: https://doi.org/10.1101/2022.03.04.22271927; this version posted March 8, 2022. The copyright holder for this preprint (which was not certified by peer review) is the author/funder, who has granted medRxiv a license to display the preprint in perpetuity. It is made available under a CC-BY-NC-ND 4.0 International license .

FIGURE LEGENDS

Figure 1: NGS reveals stability of affected genes through ALL disease progression

A. Mutated gene products identified through targeted DNA/RNA-fusion sequencing of paired diagnosis (Dx) and relapse (R) samples. Mutations detected in both Dx and R samples are represented by green boxes, mutations unique to Dx are dark purple, and R unique are light purple. CNVs are full boxes and SNVs are outlined boxes. The pie diagrams at the top summarize the number of mutations for each category for each patient. An asterisk indicates multi timepoint patients; BALL01 R2-R3-R4-R5-R5P, BALL02 Dx-R1-R2.

B. Circos plot for all mutations identified in the BCCH cohort demonstrating mutations that were Dx unique, R unique, or shared between Dx and R samples. Genes in blue text indicate genes with detected lesions in both cohorts.

C. Circos plot for all mutations identified in the SJH cohort demonstrating mutations that were Dx unique, R unique, or shared between Dx and R samples. Genes in blue text indicate genes with detected lesions in both cohorts.

D. Fraction of variants identified as D unique, R1 unique, or shared within paired samples sourced from 80 ALL patients (n= 11 from BCCH represented by squares, n= 69 from SJH represented by circles). The black bar represents the median of the population.

E. Dot plot for fraction of shared variants versus time to relapse for 80 ALL patients (n= 11 from BCCH represented by squares, n= 69 from SJH represented by circles).

F. Dot plot for fraction of shared variants separated by disease subtype for 80 ALL patients (n= 11 from BCCH represented by squares, n= 69 from SJH represented by circles). The black bar represents the median of the population.

Figure 2: Matched patient-derived leukemic cells respond similarly to variant-selected agents

A. Predicted sensitivity to targeted agents in paired Dx-R samples (or Dx-R2, R2-R3 indicated by an asterisk) taken from 80 ALL patients treated at BCCH (n=11, light blue) or SJH (n=69, dark blue). B-ALL (light brown) and T-ALL (dark brown) samples are indicated. Shared variants (green), Dx unique variants (dark purple), or R unique variants (light purple) are

medRxiv preprint doi: https://doi.org/10.1101/2022.03.04.22271927; this version posted March 8, 2022. The copyright holder for this preprint (which was not certified by peer review) is the author/funder, who has granted medRxiv a license to display the preprint in perpetuity. It is made available under a CC-BY-NC-ND 4.0 International license .

indicated. Agent-variant pairs were assigned following the strategy outlined in the Pediatric Match Trial (9).

B. Measured IC50 values for viably frozen ALL samples from patients treated at BCCH (n= 6 patients) and representative cell lines. ALL samples were co-cultured with hTERT-MSCs and separately treated with four inhibitors, MEKi, CDK4/6i, JAK/STATi, and SMOi. IC50 [µM] are colored by most sensitive in yellow to least sensitive in blue. Measurements represent the mean of n=2 replica wells from a single experiment.

C. Dot plots for IC50 [µM] values measured for primary samples or cell lines for each drug. Samples are separated based on the presence (pink) or absence (black) of a genomic variant predicted to augment drug sensitivity.

D. Correlation of IC50 [M] values measured for paired Dx and R paired samples. Individual drugs are indicated by unique identifiers. r= Pearson correlation coefficient.

Figure 3: Proteome investigation of matched specimens reveals stable levels of cancer-associated proteins and processes

A. From the list of 269 pediatric cancer associated proteins (CAPs), 141 proteins were detected in our data and 45 proteins were deemed significant (LIMMA analysis of Initial Diagnosis (Dx) samples vs. non-cancer bone marrow (BM) samples and Relapse (R) vs non-cancer BM samples (log2FC>1, p-value adjusted BH-FDR<0.05). Circos plot summarizes significantly overexpressed cancer associated proteins (CAPs).

B. Of the 45 proteins that were overexpressed, the protein expression for each protein that was overexpressed at Dx, was plotted as timepoint 1 (T1) vs timepoint 2 (T2), where T1 is the earliest timepoint available for the specimen (calculated as the log2(protein expression/the average protein expression in the non-cancer BM)). Pearson's r correlation was calculated for all sample pairs. In cases that we had multiple time-points (BALL01 and BALL02) the correlation was calculated for consecutive pairings and are represented by the different colored dots.

C. Summary of tests for equivalence (Two-one-sided t-test (TOST) for equivalence, boundaries between log2FC<-1 and log2FC>1) of protein abundance between different groups and pairings. Only statistically measurable proteins are represented. Each dot represents the mean

medRxiv preprint doi: https://doi.org/10.1101/2022.03.04.22271927; this version posted March 8, 2022. The copyright holder for this preprint (which was not certified by peer review) is the author/funder, who has granted medRxiv a license to display the preprint in perpetuity. It is made available under a CC-BY-NC-ND 4.0 International license .

equivalence or difference of all protein abundance for a pairing. Significance is assigned by mann-whitney wilcoxon test, *** indicates p-value<=0.0001.

D. Pathway enrichment analysis of the stable population of proteins represented in green and relapse enriched population of proteins represented in purple. The color of the circles indicates the enrichment FDR and size represents the number of identifications for the term.

E. Abundance of transcription factors of interest for each sample separated by timepoint (T1 or T2, black) compared to protein expression in mature B-cells (n=2 samples) isolated from peripheral blood mononuclear cells (grey).

F. Dot plots represent the log2FC of timepoint 1(T1)/timepoint 2(T2) for each of the proteins for each sample. The shaded green area indicates the stable range of -1 to 1FC. *For patients with multiple timepoints (BALL01 and BALL02) only the log2ratio of the earliest timepoint/the latest timepoint is represented for simplicity.

G. Enriched transcription factor (TF) motifs by FDR-adjusted log10 p-value. Light blue text indicates TFs that are regulated by CDK4/6 and MEK pathway. Simplified diagrams of these pathways are demonstrated below

Figure 4: Whole proteome discovery-driven analysis identifies pan-ALL protein targets

A. Correlation of log2 fold-change (FC)/non-cancer vs protein expression (log10 intensity) for all proteins in all samples (filtered for proteins identified in at least ten of seventeen samples). Dashed lines represent cut-offs for top five percent of the population for each parameter. Proteins that meet both cut-offs are colored in orange and PARP expression is represented by blue triangles.

B. Representative figure (BALL01) showing all proteins that are >log2FC of 1.7. Only the proteins that have log10 intensity >6.0 (top 5%) are colored in orange.

C. Summary of all proteins of interest (proteins that pass all cut-offs) plotted by number of samples the protein meets the indicated parameters.

D. Measured IC50 values for Olaparib or PJ34 measured against ALL or non-cancer samples from patients treated at BCCH (n= 5 non-cancer, 8 diagnostic samples, 10 relapse samples). Samples were co-cultured with hTERT-MSCs and separately treated with the two PARP1/2 inhibitors. IC50 [μM] are colored by most sensitive in yellow to least sensitive in blue.

medRxiv preprint doi: https://doi.org/10.1101/2022.03.04.22271927; this version posted March 8, 2022. The copyright holder for this preprint (which was not certified by peer review) is the author/funder, who has granted medRxiv a license to display the preprint in perpetuity. It is made available under a CC-BY-NC-ND 4.0 International license .

Measurements represent the mean of n=2 replica wells from a single experiment. Bolded Patient IDs indicate patient samples analyzed in the pan-ALL target proteomic analysis.

E. Dot plots for IC50 [μM] values for Olaparib or PJ34 measured against non-cancer specimens (black square), primary diagnostic samples (light brown circle) or primary relapse samples (black circle). Measurements represent the mean of n=2 replica wells from a single experiment. Significance (*, **) is assigned by unpaired student's t-test p-value <0.01 and p-value <0.001 respectively.

SUPPLEMENTARY FIGURE LEGENDS

Supplementary Figure S1: Genomic lesions detected in paired ALL specimens from the BCCH cohort

A-K. Line graphs for each patient treated at BCCH represent genomic lesions identified through targeted NGS in samples collected through disease progression. Only abnormal variants are plotted. CNVs are plotted by the number of copies detected and SNVs are plotted by the allelic frequency. Venn diagrams for each patient display variants that are unique to diagnosis (Dx unique), unique to relapse (R unique), or shared between samples in a progression series. An asterisk indicates the lesion is a gene-fusion detected by RNA analysis.

Supplementary Figure S2: Genomic lesions detected in paired ALL specimens from the SJH cohort

A. Bar graphs for each patient with B-ALL treated at SJH (n=49) illustrate the fraction of variants that are unique to diagnosis (Dx Unique, dark purple bars), unique to relapse (R unique, light purple bars), or shared (green bars), identified through whole genome sequencing in samples collected through disease progression. Venn diagrams are shown for selected patients to display the distribution of variants in a progression series.

B. Bar graphs for each patient with T-ALL treated at SJH (n=20) illustrate the fraction of variants that are unique to diagnosis (Dx Unique, dark purple bars), unique to relapse (R unique, light purple bars), or shared (green bars), identified through whole genome sequencing in samples collected through disease progression. Venn diagrams are shown for selected patients to display the distribution of variants in a progression series.

medRxiv preprint doi: https://doi.org/10.1101/2022.03.04.22271927; this version posted March 8, 2022. The copyright holder for this preprint (which was not certified by peer review) is the author/funder, who has granted medRxiv a license to display the preprint in perpetuity. It is made available under a CC-BY-NC-ND 4.0 International license .

Supplementary Figure S3: Dynamics of genomic lesions detected in the SJH and BCCH cohorts

A. Bar plot for the most frequent variants (top 17) detected in both Dx and paired R samples (shared) plotted as the fraction of samples containing the shared variant in each cohort (n=11 from BCCH, n=69 from SJH). Variants were detected in the BCCH cohort through targeted NGS while variants were detected in the SJH cohort through whole genome sequencing. Thus, variants that cannot be detected in the BCCH samples with the targeting sequencing assay are indicated with ^.

B. Bar plot for the most prevalent genes (top 16) detected in the combined BCCH and SJH cohorts. Variants are categorized as shared (green), Dx unique (dark purple) or R unique (light purple) and plotted as the fraction of occurrences. The total number of times the gene was identified is displayed on the right end of the bar.

C. Bar plot classifying variants (SNV, CNV, Fusion) as shared (green), Dx unique (dark purple) or R unique (light purple) and plotted as the fraction of occurrence in the BCCH cohort.

D. Dot plot for fraction of shared variants versus time to relapse for 59 B-ALL patients (n= 10 from BCCH represented by light blue circle, n= 49 from SJH represented by dark blue circles).

E. Dot plot for fraction of shared variants versus time to relapse for 21 T-ALL patients (n= 1 from BCCH represented by light blue circle, n= 20 from SJH represented by dark blue circles).

Supplementary Figure S4: Description of proteomic data filtering pipeline and quality assessment

A. Total proteins identified in each sample, prior to any filtering. The category of the sample type is listed across the top of each group.

B. Diagram of the filtering workflow to attain the final proteomics dataset utilized for subsequent analyses.

C. Upset plot for ten of the eleven standards (standard nine was removed due to a clear technical issue). Numbers reported are based on proteins quantified by a minimum of two peptides at a precursor q-value threshold of 0.5% FDR.

medRxiv preprint doi: https://doi.org/10.1101/2022.03.04.22271927; this version posted March 8, 2022. The copyright holder for this preprint (which was not certified by peer review) is the author/funder, who has granted medRxiv a license to display the preprint in perpetuity. It is made available under a CC-BY-NC-ND 4.0 International license .

D. The cv for protein quantity across the ten standards was assessed and plotted by percent coefficient of variation (CV). The darkest purple bar at the bottom represents the number of proteins with a CV of less than 10% and so on, with the lightest bar at the top representing the number of proteins with a cv greater than 50%. This fraction of proteins with cv >50% was removed from the remaining data with the assumption these are unstably quantified between samples.

E. A violon plot demonstrating the median CV of protein quantification across the ten standards (including those >50% CV). Dashed line indicates the median CV (15.7%).

Supplementary Figure S5: Evaluation of individual sample data quality

A. Bar plot to demonstrate data completeness between replica of each sample. Proteins that were identified in both replica are represented in black, dark grey represents proteins that were only identified in one of the replica, and light grey represents proteins that were entirely missing from the pair.

B. CV between replica is represented as described in panel S5 D; The darkest color bar at the bottom represents the number of proteins with a CV of less than 10% and so on, with the lightest bar at the top representing the number of proteins with a cv greater than 50%.

C. Unsupervised hierarchical clustering was performed to evaluate any bias due to batch effects. Colors represent batches. The standards are represented in grey, as these were a mix of samples from different batches.

Supplementary Figure S6: Significant cancer associated proteins (CAPs)

A. 141 proteins were tested using LIMMA (log2FC>1, p-value adjusted FDR<0.05); Initial Diagnosis (Dx) samples vs. Non-cancer BM samples on the left and Relapse (R) vs Non-cancer BM samples on the right. Proteins that are significantly over expressed in both Dx and R are colored in green and those that are unique to either Dx or R are colored in purple.

B. From the list of 269 pediatric cancer driving proteins (black circle), 141 proteins were detected in our data (gray circle) and 45 proteins were deemed significant (red circle).

C. Sixteen of the overexpressed proteins were shared between Dx and R (bottom)

D. Of the 45 proteins that were overexpressed at Dx, the protein expression for each protein at each timepoint was plotted as timepoint 1 (T1) vs timepoint 2 (T2) (calculated as the

medRxiv preprint doi: https://doi.org/10.1101/2022.03.04.22271927; this version posted March 8, 2022. The copyright holder for this preprint (which was not certified by peer review) is the author/funder, who has granted medRxiv a license to display the preprint in perpetuity. It is made available under a CC-BY-NC-ND 4.0 International license .

log2(protein expression/the average protein expression in the non-cancer bone marrow (BM) samples). A Pearson's r correlation was calculated for the entire dataset.

E. Of the 45 proteins that were under-expressed at Dx, the protein expression for each protein at each timepoint was plotted as timepoint 1 (T1) vs timepoint 2 (T2) (calculated as the log2(protein expression/the average protein expression in the non-cancer bone marrow (BM samples). A Pearson's r correlation was calculated for the entire dataset.

Supplementary Figure S7: Statistical analysis of paired samples

A. Summary of tests for differential expression and equivalence between different groups and pairings. Proteins that are statistically equivalent are represented in green (Two-one-sided t-test (TOST) for equivalence, boundaries between log2FC<-1 and log2FC>1), proteins that are statistically different are represented in purple (student's ttest p-value<0.05, log2FC>1. The bar represents the mean equivalence or difference of all protein expression for each pairing within the group.

B. Similar representation for each individual patient pairing of the group "Same patient-diff timepoints" group. The numbers on the right of each bar indicate how many statistically measurable proteins were in each pairing.

medRxiv preprint doi: https://doi.org/10.1101/2022.03.04.22271927; this version posted March 8, 2022. The copyright holder for this preprint (which was not certified by peer review) is the author/funder, who has granted medRxiv a license to display the preprint in perpetuity. It is made available under a CC-BY-NC-ND 4.0 International license .

Bibliography

1. **Ellison LF, De P, Mery LS, Grundy PE, Canadian Cancer Society's Steering Committee for Canadian Cancer Statistics. Canadian cancer statistics at a glance: cancer in children. Can Med Assoc J. 2009 Feb 17;180(4):422–424.**
2. **Sweet-Cordero EA, Biegel JA. The genomic landscape of pediatric cancers: Implications for diagnosis and treatment. Science. 2019 Mar 15;363(6432):1170–1175.**
3. **Ma X, Edmonson M, Yergeau D, Muzny DM, Hampton OA, Rusch M, et al. Rise and fall of subclones from diagnosis to relapse in pediatric B-acute lymphoblastic leukaemia. Nat Commun. 2015 Mar 19;6:6604.**
4. **Oshima K, Khiabanian H, da Silva-Almeida AC, Tzoneva G, Abate F, Ambesi-Impiombato A, et al. Mutational landscape, clonal evolution patterns, and role of RAS mutations in relapsed acute lymphoblastic leukemia. Proc Natl Acad Sci USA. 2016 Oct 4;113(40):11306–11311.**
5. **Tzoneva G, Dieck CL, Oshima K, Ambesi-Impiombato A, Sánchez-Martín M, Madubata CJ, et al. Clonal evolution mechanisms in NT5C2 mutant-relapsed acute lymphoblastic leukaemia. Nature. 2018 Jan 25;553(7689):511–514.**
6. **Schroeder MP, Bastian L, Eckert C, Gökbuget N, James AR, Tanchez JO, et al. Integrated analysis of relapsed B-cell precursor Acute Lymphoblastic Leukemia identifies subtype-specific cytokine and metabolic signatures. Sci Rep. 2019 Mar 12;9(1):4188.**
7. **Gröbner SN, Worst BC, Weischenfeldt J, Buchhalter I, Kleinheinz K, Rudneva VA, et al. The landscape of genomic alterations across childhood cancers. Nature. 2018 Mar 15;555(7696):321–327.**
8. **Ma X, Liu Y, Liu Y, Alexandrov LB, Edmonson MN, Gawad C, et al. Pan-cancer genome and transcriptome analyses of 1,699 paediatric leukaemias and solid tumours. Nature. 2018 Mar 15;555(7696):371–376.**
9. **Lorentzian A, Biegel JA, Ostrow DG, Rolf N, Liu C-C, Rassekh SR, et al. Tumor variant identification that accounts for the unique molecular landscape of pediatric malignancies. JNCI Cancer Spectr. 2018 Oct;2(4):pky079.**
10. **Waanders E, Dobson SM, Ma X, Payne-Turner D, Song G, Fan Y, et al. Genomic landscape of relapsed acute lymphoblastic leukemia. Blood. 2015 Dec 3;126(23):692–692.**
11. **Tran TH, Shah AT, Loh ML. Precision Medicine in Pediatric Oncology: Translating Genomic Discoveries into Optimized Therapies. Clin Cancer Res. 2017 Sep 15;23(18):5329–5338.**
12. **Somasundaram R, Prasad MAJ, Ungerbäck J, Sigvardsson M. Transcription factor networks in B-cell differentiation link development to acute lymphoid leukemia. Blood. 2015 Jul 9;126(2):144–152.**
13. **Lim JSJ, Tan DSP. Understanding resistance mechanisms and expanding the therapeutic utility of PARP inhibitors. Cancers (Basel). 2017 Aug 22;9(8).**
14. **Rouleau M, Patel A, Hendzel MJ, Kaufmann SH, Poirier GG. PARP inhibition: PARP1 and beyond. Nat Rev Cancer. 2010 Apr;10(4):293–301.**
15. **Langenberg KPS, Looze EJ, Molenaar JJ. The landscape of pediatric precision oncology: program design, actionable alterations, and clinical trial development. Cancers (Basel). 2021 Aug 27;13(17).**

medRxiv preprint doi: https://doi.org/10.1101/2022.03.04.22271927; this version posted March 8, 2022. The copyright holder for this preprint (which was not certified by peer review) is the author/funder, who has granted medRxiv a license to display the preprint in perpetuity. It is made available under a CC-BY-NC-ND 4.0 International license .

16. **Wong M, Mayoh C, Lau LMS, Khuong-Quang D-A, Pinese M, Kumar A, et al. Whole genome, transcriptome and methylome profiling enhances actionable target discovery in high-risk pediatric cancer. Nat Med. 2020 Nov;26(11):1742–1753.**
17. **van Tilburg CM, Pfaff E, Pajtler KW, Langenberg KPS, Fiesel P, Jones BC, et al. The Pediatric Precision Oncology INFORM Registry: Clinical Outcome and Benefit for Patients with Very High-Evidence Targets. Cancer Discov. 2021 Nov;11(11):2764–2779.**
18. **Andersson N, Bakker B, Karlsson J, Valind A, Holmquist Mengelbier L, Spierings DCJ, et al. Extensive Clonal Branching Shapes the Evolutionary History of High-Risk Pediatric Cancers. Cancer Res. 2020 Apr 1;80(7):1512–1523.**
19. **Karlsson J, Valind A, Holmquist Mengelbier L, Bredin S, Cornmark L, Jansson C, et al. Four evolutionary trajectories underlie genetic intratumoral variation in childhood cancer. Nat Genet. 2018 Jul;50(7):944–950.**
20. **Sayyab S, Lundmark A, Larsson M, Ringnér M, Nystedt S, Marincevic-Zuniga Y, et al. Mutational patterns and clonal evolution from diagnosis to relapse in pediatric acute lymphoblastic leukemia. Sci Rep. 2021 Aug 6;11(1):15988.**
21. **Matheson EC, Thomas H, Case M, Blair H, Jackson RK, Masic D, et al. Glucocorticoids and selumetinib are highly synergistic in RAS pathway-mutated childhood acute lymphoblastic leukemia through upregulation of BIM. Haematologica. 2019 Sep;104(9):1804–1811.**
22. **Irving J, Matheson E, Minto L, Blair H, Case M, Halsey C, et al. Ras pathway mutations are prevalent in relapsed childhood acute lymphoblastic leukemia and confer sensitivity to MEK inhibition. Blood. 2014 Nov 27;124(23):3420–3430.**
23. **Frisone D, Charrier M, Clement S, Christinat Y, Thouvenin L, Homicsko K, et al. Durable response to palbociclib and letrozole in ovarian cancer with CDKN2A loss. Cancer Biol Ther. 2020;21(3):197–202.**
24. **Goel S, DeCristo MJ, McAllister SS, Zhao JJ. CDK4/6 inhibition in cancer: beyond cell cycle arrest. Trends Cell Biol. 2018 Jul 27;28(11):911–925.**
25. **Gong X, Litchfield LM, Webster Y, Chio L-C, Wong SS, Stewart TR, et al. Genomic Aberrations that Activate D-type Cyclins Are Associated with Enhanced Sensitivity to the CDK4 and CDK6 Inhibitor Abemaciclib. Cancer Cell. 2017 Dec 11;32(6):761–776.e6.**
26. **Sherr CJ, Beach D, Shapiro GI. Targeting CDK4 and CDK6: from discovery to therapy. Cancer Discov. 2016 Apr;6(4):353–367.**
27. **Chae YK, Pan AP, Davis AA, Patel SP, Carneiro BA, Kurzrock R, et al. Path toward Precision Oncology: Review of Targeted Therapy Studies and Tools to Aid in Defining "Actionability" of a Molecular Lesion and Patient Management Support. Mol Cancer Ther. 2017 Dec;16(12):2645–2655.**
28. **Grover SA, Alcindor T, Berman JN, Chan JA, Denburg AE, Deyell RJ, et al. Abstract 636: PROFYLE: The pan-Canadian precision oncology program for children, adolescents and young adults with hard-to-treat cancer. Clinical Research (Excluding Clinical Trials). American Association for Cancer Research; 2021. p. 636–636.**
29. **Rikova K, Guo A, Zeng Q, Possemato A, Yu J, Haack H, et al. Global survey of phosphotyrosine signaling identifies oncogenic kinases in lung cancer. Cell. 2007 Dec 14;131(6):1190–1203.**

medRxiv preprint doi: https://doi.org/10.1101/2022.03.04.22271927; this version posted March 8, 2022. The copyright holder for this preprint (which was not certified by peer review) is the author/funder, who has granted medRxiv a license to display the preprint in perpetuity. It is made available under a CC-BY-NC-ND 4.0 International license .

30. Doll S, Gnad F, Mann M. The Case for Proteomics and Phospho-Proteomics in Personalized Cancer Medicine. Proteomics Clin Appl. 2019;13(2):e1800113.

31. Coscia F, Lengyel E, Duraiswamy J, Ashcroft B, Bassani-Sternberg M, Wierer M, et al. Multi-level Proteomics Identifies CT45 as a Chemosensitivity Mediator and Immunotherapy Target in Ovarian Cancer. Cell. 2018 Sep 20;175(1):159–170.e16.

32. Frismantas V, Dobay MP, Rinaldi A, Tchinda J, Dunn SH, Kunz J, et al. Ex vivo drug response profiling detects recurrent sensitivity patterns in drug-resistant acute lymphoblastic leukemia. Blood. 2017 Mar 16;129(11):e26–e37.

33. Hughes CS, Moggridge S, Müller T, Sorensen PH, Morin GB, Krijgsveld J. Single-pot, solid-phase-enhanced sample preparation for proteomics experiments. Nat Protoc. 2019 Jan;14(1):68–85.

34. Reimand J, Isserlin R, Voisin V, Kucera M, Tannus-Lopes C, Rostamianfar A, et al. Pathway enrichment analysis and visualization of omics data using g:Profiler, GSEA, Cytoscape and EnrichmentMap. Nat Protoc. 2019 Feb;14(2):482–517.

35. Shannon P, Markiel A, Ozier O, Baliga NS, Wang JT, Ramage D, et al. Cytoscape: a software environment for integrated models of biomolecular interaction networks. Genome Res. 2003 Nov;13(11):2498–2504.